J. Fluid Mech. (2022), *vol*. 947, A9, doi:10.1017/jfm.2022.636

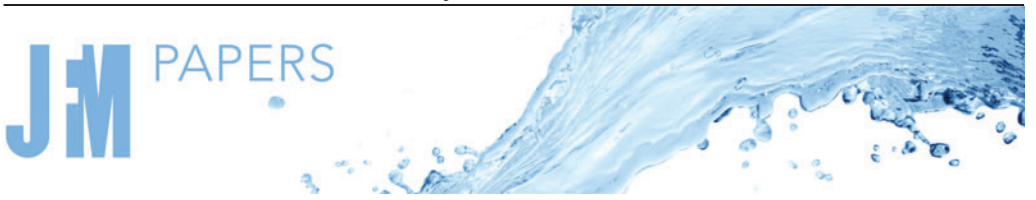

Numerical simulation of bubble dynamics and segregation in binary heptane/dodecane mixtures

J.M. Bermudez-Graterol[1],† **and R. Skoda**[1]

[1]Chair of Hydraulic Fluid Machinery, Ruhr University Bochum, Universitätsstr. 150, 44801 Bochum, Germany

(Received 21 September 2021; revised 10 June 2022; accepted 12 July 2022)

A mathematical model for the simulation of spherical bubble dynamics in binary alkane mixtures is presented. Detailed heat and mass transfer and phase transition are resolved, and air absorption and desorption are considered. As example mixtures, high-volatile heptane and low-volatile dodecane are investigated. The low-volatile component shows a convective counter-intuitive mass transport opposite to the diffusion flux. A staggered mass flux of heptane and dodecane is associated with a local segregation of mixture components in the surrounding liquid and a distinctive species distribution within the bubble. A comparative study with a pseudo-fluid where alkane species interdiffusion is absent and whose components cannot segregate reveals that for an oscillating bubble, the local segregation hardly affects bubble dynamics, while for a continuously growing bubble in a superheated liquid, the growth rate is considerably affected, particularly for a low heptane mixture percentage. This study demonstrates limitations of treating mixtures by a single-component surrogate fluid and may serve as a starting point for the development of multi-component cavitation models for computational fluid dynamics applications in real fluid mixtures as, e.g. fuels or hydraulic oils.

Key words: bubble dynamics, cavitation

1. Introduction

Cavitation is associated with the formation, growth, oscillation and collapse of vapour and gas filled bubbles due to rapid changes of the pressure in the surrounding liquid. In hydraulic systems, e.g. fuel injection or oil-hydraulics devices, cavitation may have serious complications as generation of sound, vibration and cavitation erosion. One peculiarity of hydraulic systems is the working fluid in terms of e.g. fuel or hydraulic oil, which may consist of several hundred components. Thermophysical properties thus depend, beyond local temperature and pressure, also on the local mixture composition. In recent

† Email address for correspondence: jean.bermudezgraterol@ruhr-uni-bochum.de

three-dimensional computational fluid dynamics (3-D CFD) approaches of cavitating flow in hydraulic systems, single-component surrogate fluids have been utilized to model the real mixtures. For example, Schnerr *et al.* (2006) utilized water as a surrogate. Further studies, e.g. Giannadakis, Gavaises & Arcoumanis (2008*a*), Giannadakis *et al.* (2008*b*), Skoda *et al.* (2012), Theodorakakos *et al.* (2014), Koukouvinis *et al.* (2016) and Oerley *et al.* (2015), to cite only a few, applied the properties of dodecane, decane, heptane or a diesel-like single-component surrogate fluid to model real diesel fuel. For hydraulic oil, also single-component surrogate fluids were utilized (Schrank, Murrenhoff & Stammen 2013).

The liquid and vapour phases of single-component surrogate fluids are based on a homogeneous, i.e. spatially and temporally constant, mixture. As for pure substances, the properties of the surrogate fluid are dependent only on temperature and pressure. A prospective local change of properties due to local segregation of mixture components at phase interfaces in cavitating flow is inherently neglected. In fact, in the transmission light study by Dorofeeva, Thomas & Dunn (2009) and Dunn *et al.* (2010) on cavitating kerosene flow in a Venturi nozzle, a significant local fuel segregation was observed. A comparison to pure fluids in terms of water, decane and dodecane revealed significant differences of the cavitation void structures in kerosene. Kerosene is a classical real fuel mixture with a multitude of components, essentially consisting of alkanes and aromatics. The vapour saturation pressure of the separate components varies by three orders of magnitude (Dunn *et al.* 2010), so the particular cavitation structures were traced back to a temporally staggered evaporation and re-condensation of the individual kerosene components (Dorofeeva *et al.* 2009; Dunn *et al.* 2010). However, due to inherent limitations of the optical measurement techniques, it remained unclear if the segregation of fuel components or the segregation of fuel and dissolved air by air desorption was the dominating observation, and it may be speculated that both effects arise simultaneously. This observation motivated us to launch this simulation study on local segregation of fuel components associated with bubble dynamics and cavitation.

In 3-D CFD methods, mass transfer cavitation models, as proposed e.g. by Schnerr & Sauer (2001) and Zwart, Gerber & Belamri (2014), are combined with the Navier–Stokes equations for the evaluation of phase transition from liquid to vaporous phase and vice versa. This model class is based on simplified fundamentals of bubble dynamics and mostly uses the simple Rayleigh equation (Plesset & Prosperetti 1977) to evaluate the mass transfer rate. So far, available mass transfer cavitation models are based on single-component fluids only, to the best knowledge of the authors. Therefore, when fluid mixtures are considered by single-component surrogates, only bulk properties of the mixture enter the cavitation model and the governing equations. In fact, it can be concluded that the fuel segregation during cavitation, observed e.g. by Dorofeeva *et al.* (2009) and Dunn *et al.* (2010), cannot be reproduced with available mass transfer cavitation models, a fact that reveals inherent limitations of state-of-the-art 3-D CFD methods. Another interesting cavitation model approach is based on statistical associating fluid theory (SAFT) (Rokni *et al.* 2019; Vidal *et al.* 2020; Kolovos *et al.* 2021) and allows for the description of local changes of phase composition and therefore of fuel mixture properties changes. However, this approach is based on thermodynamic equilibrium, and a local transport of the mixture components is inherently not accounted for. Thus an important step towards a multi-component mass transfer cavitation model demands a reconsideration of local transport processes around single bubbles for a description of a staggered phase transition of low- and high-volatile mixture components, which has not been considered until now and is therefore the subject of this study.

Beyond the segregation of fuel components, desorption of non-condensable gas may occur during dynamics of a single bubble and should be considered in the modelling approach, together with the fuel segregation. Thus far, available studies focused only on single-fluid/non-condensable gas systems, and most of them considered water and air. Approximations with the spatial transport of either vapour or non-condensable gas have been proposed by Nigmatulin & Khabeev (1975) for the former, or Nigmatulin & Khabeev (1974), Arefmanesh, Advani & Michaelides (1992), Naji Meidani & Hasan (1997, 2004), Klein & Iben (2010) and Vachaparambil & Einarsrud (2020) for the latter. Sochard, Wilhelm & Delmas (1998) have also considered gas–vapour interdiffusion within the bubble as well as the liquid–vapour phase transition, i.e. evaporation and condensation across the interface, but gas diffusion across the interface was neglected. Kamath & Prosperetti (1989) considered interdiffusing non-condensable gases in the bubble interior. However, no phase transition over the interface and no vapour content in the bubble were considered. Matsumoto & Takemura (1994), Takemura & Matsumoto (1994) and Matsumoto & Yoshizawa (2005) solved the Navier–Stokes equations with radial resolution of the concentration and temperature field within and outside of the bubble, while a Rayleigh–Plesset equation considering mass transfer (Fujikawa & Akamatsu 1980) determined the time-dependent bubble wall position. Air diffusion and the interface condition for air were modelled by Fick's and Henry's laws, respectively. Phase transition was approximated as a thermal non-equilibrium process by the Hertz–Knudsen relation (Persad & Ward 2016), while Bermudez-Graterol, Nickaeen & Skoda (2021) could show that an equilibrium condition hardly changed the bubble dynamics even during the collapse phase. Jinbo *et al.* (2015) used an approach similar to that of Matsumoto & Takemura (1994) but resolved the bubble interface with a level-set and ghost fluid method. Yamamoto *et al.* (2019) figured out by a molecular dynamics method that a small amount of non-condensable gas strongly affects the temperature field inside the collapsing bubble. Zein, Hantke & Warnecke (2013) performed 3-D simulations with mass and heat transfer together with the transport of vapour as well as air. Assuming homobaricity within the bubble – i.e. the bubble pressure is spatially homogeneous and dependent only on time – Nigmatulin, Khabeev & Nagiev (1981) and Kawashima & Kameda (2008), and more recently Hao, Zhang & Prosperetti (2017) and Bermudez-Graterol *et al.* (2021), evaluated the spatial velocity distribution within the bubble as well as the temporal evolution of the (spatially constant) bubble pressure by an analytical expression that was derived from the energy equation. In the surrounding liquid, the flow was irrotational and thus potential. A similar approach has been used by other authors (Prosperetti 1991; Soh & Karimi 1996; Delale & Pasinlioğlu 2015; Ali & Ake 2016). Hao *et al.* (2017) pointed out the effect of bubble content, in terms of both vapour and non-condensable gas, on bubble dynamics. These cited studies are based on pure water/non-condensable gas (mostly air) systems, and no other fluids than water and, least of all, fluid mixtures have been considered.

Studies on bubble dynamics with fluid mixtures and a systematic fluid variation are rare. Plesset (1970) performed experiments on cavitation erosion in an ultrasound device with binary fluid mixtures of water with acetone, formamide, ethanol or glycerol, and concluded that mixture viscosity and air content affected the erosion rate. Huang & Mohamad (2009) performed single-bubble simulations to reproduce the binary mixture measurements of Plesset (1970). Their model was based on the Rayleigh–Plesset equation for a single-component surrogate fluid, where linear mixture rules for obtaining the surrogate bulk properties were applied. Thus local fluid segregation was inherently neglected by Huang & Mohamad (2009). Regarding wall heat transfer simulations on pool boiling of binary mixtures (Wang, Xie & Tan 1996*a*,*b*), the effect of segregation

was taken into account via different concentrations of fluid components both within and outside the bubble. However, the spatial and temporal variation of the mixture composition was not considered. By solving the Navier–Stokes equations, Storey & Szeri (1999, 2000) studied sonoluminescence by a segregation of helium and argon as well as argon and steam, and resolved the spatial and temporal distribution of the components within the bubble. During bubble collapse, an enhanced segregation and a concentration of water or helium, respectively, was observed towards the bubble centre. Beyond diffusion due to concentration gradients, thermal diffusion due to temperature gradients affected the in-bubble flow during a later stage of bubble collapse. In contrast, pressure diffusion due to pressure gradients had an appreciable effect only in a very short time interval, so its effect was considered inessential (Storey & Szeri 1999, 2000). A prospective segregation of fluid in the surrounding liquid was not investigated by Storey & Szeri (1999, 2000).

Thus the local segregation of fluid mixture components during bubble dynamics has hardly been considered in previous studies. In fact, the studies by Storey & Szeri (1999, 2000) on helium, argon and steam are the only ones of which we are aware, and even these are restricted to segregation of gaseous components within the bubble, while a segregation of liquid mixture components outside the bubble was not considered. A completely different situation occurs for droplet evaporation. Local segregation of liquid mixture components in fuel droplets has been investigated widely by multi-component evaporation models for gasoline (Gartung, Arndt & Seibel 2002), diesel (Lippert & Reitz 1997), biodiesel fuels or ethanol–gasoline mixtures (Hallett & Beauchamp-Kiss 2010; Hallett & Legault 2011; Zhang & Kong 2012; Bader, Keller & Hasse 2013), to list only a few. Sazhin *et al.* (2011) provided an overview of multi-component models for fuel droplet evaporation. In more recent studies on binary mixtures, Li *et al.* (2018, 2020) reported evaporation-triggered segregation in 1,2-hexanediol–water droplets, and Millán-Merino, Fernández-Tarrazo & Sánchez-Sanz (2021) observed higher vaporization rates with increasing ambient humidity for ethanol–water droplets. The mixture segregation of the droplet is associated with strongly different and temporally staggered mass flow rates of the individual mixture components at the phase interface. The evaporation rate of high-volatile components is larger than that of low-volatile components, leading to a densification of the liquid fuel within the droplet. The opposite trend was observed during condensation. In the liquid phase within the droplet as well as in the surrounding vaporous phase, a temporal and spatial variation of the local fuel composition occurs that again affects the mixture state and transport properties, e.g. for cold environmental conditions (Lippert & Reitz 1997) or flash boiling (Ra & Reitz 2003; Yang & Reitz 2009). We assume that such processes occur also during different stages of bubble dynamics, which has, however, not been studied yet. Therefore, the subject of the present study is the assessment of local segregation of fluid mixtures by single-bubble flow simulations. Thereby, we pay particular attention to the peculiarities of multi-component transport in comparison with a conventional single-component bulk fluid treatment (termed a pseudo-fluid in this study). We content ourselves with binary mixtures in this first study on this topic, and choose heptane (C7H16) and dodecane (C12H26) as high- and low-volatile components, respectively, since these fluids are common components of real fuels. Since no single-bubble simulation model for fluid mixtures has been presented before, we present a complete governing equation set that comprises an extension of our preceding study on water–air systems (Bermudez-Graterol *et al.* 2021). No experimental data on mixture bubble dynamics are available, so we must content ourselves with a validation on bubble growth in water. However, the simulation results will provide an insight into the local heat,

mass and phase transfer processes of mixture bubble dynamics, and hence may serve as a basis for a purposeful experimental set-up in future studies.

The paper is organized as follows. In §§ 2 and 3, the mathematical model and its numerical solution method are presented. In § 4, results of two example bubble dynamics scenarios are presented: first, bubble oscillation after a rapid pressure drop is investigated in § 4.1; and second, continuous bubble growth in superheated liquid is studied in § 4.2. We finalize the paper with our conclusions and outlook in § 5.

2. Mathematical model formulation

2.1. *Model outline and notations*

The mathematical model of a single spherical bubble is based on our preceding study on water–air mixtures (Bermudez-Graterol *et al.* 2021). Homobaricity is assumed within (but not outside) the bubble, which is justified for $|\dot{R}| \ll a^G$ (Nigmatulin *et al.* 1981), where a^G is the speed of sound. This condition is fulfilled for any test case in this study. Homobaricity allows the omission of the full Navier–Stokes equations. Instead of solving the Navier–Stokes equations, the velocity field and the pressure within the bubble are obtained by the energy equation. Outside the bubble, the velocity and pressure fields are obtained by noting that the flow is irrotational. The homobaricity assumption reduces considerably the computational effort and thereby opens the opportunity to embed a large number of single bubbles in a 3-D Euler–Lagrange framework in future studies, which will be picked up in the outlook at the end of this paper. Binary heptane/dodecane mixtures are investigated, referred to as fuel in what follows, together with air. Air is treated as a single-component pseudo-fluid, so the model comprises three species in total. Thus the bubble contains a mixture of vaporous heptane and dodecane as well as non-condensable gas, i.e. air, which are assumed to be thermally and calorically ideal. The bubble is surrounded with an infinite amount of a liquid heptane/dodecane mixture, in which air is dissolved. Both within (superscript $\gamma = G$) and outside (superscript $\gamma = L$) the bubble, mixture values (subscript m) are evaluated by a mass fraction weight $y_\alpha^\gamma = \rho_\alpha^\gamma / \rho_m^\gamma$, where ρ is the mass density, and index α means either heptane (subscript $\alpha = Hep$), dodecane (subscript $\alpha = Dod$) or air (subscript $\alpha = Air$). The species add to 1 when α is summed over all $N_S = 3$ species:

$$\sum_{\alpha=1}^{N_S} y_\alpha^\gamma = y_{Hep}^\gamma + y_{Dod}^\gamma + y_{Air}^\gamma = 1. \tag{2.1}$$

In what follows, the mathematical model is outlined, while details are presented in Appendix A. The assumptions made are listed in § A.1.

2.2. *Governing equations*

The governing equations are solved in spherical coordinates. For both the gaseous bubble interior and its surrounding liquid, the mass conservation of mixture m and its components α reads

$$\frac{\partial(\rho_m^\gamma)}{\partial t} + \frac{1}{r^2}\frac{\partial}{\partial r}(r^2 \rho_m^\gamma u^\gamma) = 0, \tag{2.2}$$

$$\frac{\partial(\rho_m^\gamma y_\alpha^\gamma)}{\partial t} + \frac{1}{r^2}\frac{\partial}{\partial r}(r^2 \rho_m^\gamma y_\alpha^\gamma u^\gamma) = \frac{1}{r^2}\frac{\partial}{\partial r}\left(r^2 \rho_m^\gamma D_\alpha^\gamma \frac{\partial y_\alpha^\gamma}{\partial r}\right), \tag{2.3}$$

where u is the absolute velocity, D is the diffusion coefficient, $\alpha = Hep$, Dod or Air, and $\gamma = G$ or L.

2.2.1. *Within bubble*

Mixture pressure p^G is assumed to fulfil Dalton's law, $p^G = p^G_{Hep} + p^G_{Dod} + p^G_{Air}$. For a thermally ideal gas, it is evaluated by

$$p^G = \rho_m^G \mathcal{R}_m T^G, \tag{2.4}$$

where $\mathcal{R}_m$ and T^G correspond to the mixture gas constant and the temperature, respectively.

Employing the homobaricity assumption $\partial p^G/\partial r = 0$, an integro-differential expression for the velocity profile is obtained from energy conservation:

$$u^G = -\frac{r}{3p^G}\frac{\mathrm{d}p^G}{\mathrm{d}t} + \frac{1}{r^2 p^G}\int_0^r \left(G(r) + \frac{\mathcal{R}_m}{c^G_{p,m}}\frac{\mathrm{d}p^G}{\mathrm{d}t}\right) r^2\,\mathrm{d}r, \tag{2.5}$$

with

$$G(r) = \frac{\mathcal{R}_m}{c^G_{p,m}}\left\{\frac{1}{r^2}\frac{\partial}{\partial r}\left(r^2 \rho_m^G T^G \sum_{\alpha=1}^{N_S} \mathcal{R}_\alpha D_\alpha^G \frac{\partial y_\alpha^G}{\partial r}\right) + \frac{1}{r^2}\frac{\partial}{\partial r}\left(r^2 \lambda_m^G \frac{\partial T^G}{\partial r}\right) + \frac{T^G c^G_{v,m}}{\mathcal{R}_m}\frac{1}{r^2}\sum_{\alpha=1}^{N_S}\mathcal{R}_\alpha \frac{\partial}{\partial r}\left(r^2 \rho_m^G D_\alpha^G \frac{\partial y_\alpha^G}{\partial r}\right) + \rho_m^G \frac{\partial T^G}{\partial r}\sum_{\alpha=1}^{N_S} c^G_{v,\alpha} D_\alpha^G \frac{\partial y_\alpha^G}{\partial r}\right\}. \tag{2.6}$$

By evaluating (2.5) at the bubble wall $r = R$ and rearranging, an expression for the temporal pressure evolution within the bubble is obtained:

$$\frac{\mathrm{d}p^G}{\mathrm{d}t} = \frac{-R^2 p^G u_w^G + \displaystyle\int_0^R G(r)\, r^2\,\mathrm{d}r}{\dfrac{R^3}{3} - \displaystyle\int_0^R \frac{\mathcal{R}_m}{c^G_{p,m}} r^2\,\mathrm{d}r}. \tag{2.7}$$

More details are provided in § A.2. An even more detailed derivation of the governing equations for the velocity field and the pressure has been provided in Nickaeen (2020) for a water–air system. As a main advance provided in this study, we have extended the equations from water to discrete alkane mixtures, resulting in (2.5)–(2.7). The velocity u_w^G at the gaseous side of the bubble wall is obtained by the conservation of mass flux $\dot{m}'' = \dot{m}''_{Hep} + \dot{m}''_{Dod} + \dot{m}''_{Air}$ through the bubble wall. The mass flux reads $\dot{m}'' = \rho^G_{m,w}(\dot{R} - u_w^G)$ and is assumed positive when flowing into the bubble. Thus

$$u_w^G = \dot{R} - \frac{\dot{m}''}{\rho^G_{m,w}}. \tag{2.8}$$

Note that $\dot{m}''$ corresponds to the area-specific mass flux, and the actual mass flow $\dot{m}_\alpha$ is obtained by $\dot{m}_\alpha = A_B\,\dot{m}''_\alpha$ with the bubble area $A_B = 4\pi R^2$. Assuming ideal gas, energy

conservation reads

$$\rho_m^G c_{p,m}^G \frac{\partial T^G}{\partial t} = -\rho_m^G c_{p,m}^G u^G \frac{\partial T^G}{\partial r} + \frac{1}{r^2}\frac{\partial}{\partial r}\left(r^2 \lambda_m^G \frac{\partial T^G}{\partial r}\right) + \rho_m^G \frac{\partial T^G}{\partial r} \sum_{\alpha=1}^{N_S} c_{p,\alpha}^G D_\alpha^G \frac{\partial y_\alpha^G}{\partial r} + \frac{\mathrm{d}p^G}{\mathrm{d}t}. \tag{2.9}$$

With (2.3) ($\gamma = G$), (2.4), (2.5), (2.7) and (2.9), an equation set for the evaluation of the gas field variables y_α^G, ρ_m^G, u^G and T^G, as well as the time-dependent pressure p^G, is available.

2.2.2. *Within liquid*

Neglecting viscous effects, the energy equation reads

$$\rho_m^L c_m^L \left(\frac{\partial T^L}{\partial t} + u^L \frac{\partial T^L}{\partial r}\right) = \frac{1}{r^2}\frac{\partial}{\partial r}\left(r^2 \lambda_m^L \frac{\partial T^L}{\partial r}\right) + \rho_m^L \sum_{\alpha=1}^{N_S} D_\alpha^L \frac{\partial y_\alpha^L}{\partial r}\frac{\partial h_\alpha^L}{\partial r}, \tag{2.10}$$

where c_m^L is the specific heat of the liquid mixture. Liquid density ρ_m^L is variable due to a varying mixture composition in the surrounding liquid phase. However, since the densities of pure liquid heptane and dodecane deviate by less than 10 %, and liquid density variations due to variable mixing ratio are therefore small, we prefer the incompressible formulation of the energy equation in terms of (2.10) that does not include the work done by the pressure force, according to Bird, Stewart & Lightfoot (1960). Nevertheless, slight variations of ρ_m^L are considered by a mixture equation of state that will be introduced in § A.4.1. This approximation is equivalent to the assumption that liquid compressibility effects due to flow dynamics are neglected in (2.10), and only a locally varying fuel composition accounts for liquid density variations. The second term on the right-hand side of (2.10) corresponds to the heat transport by each of the diffusing species. The spatial change of the enthalpy of the separate species h_α^L is evaluated by

$$\frac{\partial h_\alpha^L}{\partial r} = c_\alpha^L \frac{\partial T^L}{\partial r} + \frac{1}{\rho_\alpha^L}\frac{\partial p^L}{\partial r}. \tag{2.11}$$

The liquid pressure p^L distribution is evaluated by Bernoulli's equation, noting that we have a potential flow around the bubble. A detailed description of the evaluation of p^L is provided in § 1 of the supplementary material.

The integral momentum balance is considered by a modified form of the Rayleigh–Plesset equation (Fujikawa & Akamatsu 1980) that takes into account the mass flux $\dot{m}''$ across the bubble wall:

$$R\ddot{R} + \frac{3}{2}\dot{R}^2 - \frac{\ddot{m}'' R}{\rho_{m,w}^L} - \frac{\dot{m}''}{\rho_{m,w}^L}\left(\dot{R} + \frac{1}{2}\frac{\dot{m}''}{\rho_{m,w}^L}\right) + \left(\frac{p_\infty^L - p_w^L}{\rho_{m,w}^L}\right) = 0. \tag{2.12}$$

Equation (2.12) governs the bubble interface location in terms of the temporal progression of R, where $\dot{\square}$ denotes the time derivative, and $\ddot{\square}$ denotes the second time derivative. In (2.12), p_∞^L can be understood as the driving variable of the bubble motion. Note that although we do not resolve spatially the momentum conservation

equation, momentum balance is considered integrally by the solution of (2.12). This equation has been formulated by Fujikawa & Akamatsu (1980), taking into account liquid compressibility effects. We have adopted the incompressible form here. Assuming incompressibility has been verified in preliminary test simulations, for the test cases considered in § 4. By the terms including the mass flux $\dot{m}''$ in (2.12), local heat and mass transport are coupled to bubble dynamics. The mass flux $\dot{m}''$ is composed of its individual components $\dot{m}''_{Hep}$, $\dot{m}''_{Dod}$ and $\dot{m}''_{Air}$, which govern fuel segregation in the proximity of the bubble wall. It is interesting to note that for the test cases considered, the inclusion of $\dot{m}''$ and $\ddot{m}''$ in (2.12) virtually does not affect bubble dynamics, so it can be omitted in the Rayleigh–Plesset equation.

By the same reasoning on mass conservation as applied to the velocity at the gas side of the bubble wall in terms of (2.8), a relation for the liquid side velocity is obtained:

$$u^L_w = \dot{R} - \frac{\dot{m}''}{\rho^L_{m,w}}. \tag{2.13}$$

The velocity field in the liquid surrounding the bubble is approximated by the mass conservation, neglecting small variations of the liquid density:

$$u^L = \frac{R^2}{r^2}\left(\dot{R} - \frac{\dot{m}''}{\rho^L_{m,w}}\right). \tag{2.14}$$

Equation (2.14) corresponds to an incompressible and irrotational flow.

With (2.3) ($\gamma = L$), (2.10), (2.12) and (2.14), an equation set for the evaluation of the liquid field variables y^L_α, T^L and u^L, as well as the time-dependent bubble radius R, has been obtained.

2.3. *Boundary conditions*

2.3.1. *At the bubble centre and in the liquid far field*

The bubble centre is assumed to be motionless, and all variables approach the centre with a vanishing gradient. Thus Neumann boundary conditions are formulated for the dependent variables:

$$\left.\frac{\partial \rho^G_m}{\partial r}\right|_{r=0} = 0, \quad \left.\frac{\partial y^G_\alpha}{\partial r}\right|_{r=0} = 0, \quad \left.\frac{\partial u^G}{\partial r}\right|_{r=0} = 0, \quad \left.\frac{\partial T^G}{\partial r}\right|_{r=0} = 0. \tag{2.15a–d}$$

At the outer liquid boundary of the computational domain, referred to as the liquid far field (index ∞), u^L is readily available by the kinematic condition (2.14) and does not demand any further boundary treatment. In the liquid far field, y^L_α and T^L remain at their initial values (which is explicated in § 2.4) and are formulated as Dirichlet conditions:

$$y^L_{\alpha,\infty} = y^L_{\alpha,0}, \quad T^L_\infty = T^L_0. \tag{2.16a,b}$$

In the Rayleigh–Plesset equation (2.12), p^L_∞ is prescribed explicitly as a function of time.

2.3.2. *At the bubble wall*

For the evaluation of the pressure p_w^L at the liquid side of the bubble wall in (2.12), the relation between bubble pressure p^G and liquid pressure p_w^L is given by

$$p_w^L = p^G - \frac{2\sigma_m}{R} - \frac{(\dot{m}'')^2(\rho_{m,w}^G - \rho_{m,w}^L)}{\rho_{m,w}^G \rho_{m,w}^L}, \tag{2.17}$$

where σ_m is the surface tension of the mixture. Equation (2.17) does not include the effect of viscosity since we found that it has virtually no effect for the test cases considered. According to Fujikawa & Akamatsu (1980), the last term on the right-hand side of (2.17) can be neglected, which we have also verified in preliminary tests.

Thermal and phase equilibrium is assumed and enables a straightforward formulation of mixture boundary conditions at the bubble wall. Thermal equilibrium means that the temperatures at both sides of the bubble wall are equal:

$$T_w^G = T_w^L. \tag{2.18}$$

Phase equilibrium means that the liquid and vapour phases have the same chemical potential. At low pressures, assuming that the vapour behaves like an ideal gas, the following relation is often used to describe the vapour–liquid equilibrium (Koretsky 2012):

$$\gamma_\alpha x_{\alpha,w}^L p_\alpha^{Sat}|_{T_w^L} = x_{\alpha,w}^G p^G, \tag{2.19}$$

with mole fractions $x_{\alpha,w}^L$ and $x_{\alpha,w}^G$, activity coefficients γ_α, and $\alpha = Hep$ or Dod. The activity coefficients account for the deviation from ideal solution caused by changes in composition. For chemically similar species, the numerical value of γ_α is close to 1. Activity coefficients can be obtained by using models for the excess Gibbs energy, such as, the Wilson equation, NRTL or UNIQUAC (Gmehling *et al.* 2012). Recognizing the chemical similarity of alkane species heptane and dodecane, we set γ_α to be equal to 1 for simplicity. With $\gamma_\alpha = 1$ in (2.19), we obtain Raoult's law. A validation with experimentally measured vapour–liquid equilibria by Maia de Oliveira *et al.* (2002) is presented in § A.3.

The heat balance reads

$$q_w^L - L_m(\dot{m}_{Hep}'' + \dot{m}_{Dod}'') = q_w^G, \tag{2.20}$$

where L_m is the latent heat of the fuel mixture. The heat transport by each of the diffusing components has been neglected in (2.20) because it is small, as was verified by preliminary tests. The heat flux is evaluated by Fourier's law in terms of $q_w^L = \lambda_{m,w}^L(\partial T^L/\partial r)|_w$ and $q_w^G = \lambda_{m,w}^G(\partial T^G/\partial r)|_w$, and the mixture thermal conductivities λ_m^L and λ_m^G are defined in §§ 2.5 and A.4.

The mass balance for species α at the bubble wall reads, where $\alpha = Hep$, Dod or Air,

$$\dot{m}_\alpha'' = \dot{m}_{\alpha,conv}'' + \dot{m}_{\alpha,diff}''. \tag{2.21}$$

The first term on the right-hand side of (2.21) is the convective mass flux $\dot{m}_{\alpha,conv}'' = -\rho_{m,w}^\gamma y_{\alpha,w}^\gamma(u_w^\gamma - \dot{R})$ of species α in the relative frame of reference, which means relative to the moving bubble wall. The second term, $\dot{m}_{\alpha,diff}'' = \rho_{m,w}^\gamma D_{\alpha,w}^\gamma(\partial y_\alpha^\gamma/\partial r)|_w$, corresponds to diffusion of species α. After inserting (2.8) and (2.13) into (2.21) and rearranging, we

obtain the mass balance equations for the gas ($\gamma = G$) and liquid ($\gamma = L$) side, with α and β as *Hep*, *Dod* or *Air*:

$$\dot{m}''_\alpha(1 - y^\gamma_{\alpha,w}) - y^\gamma_{\alpha,w} \sum_{\substack{\beta=1 \\ \beta \neq \alpha}}^{N_S} \dot{m}''_\beta = \rho^\gamma_{m,w} D^\gamma_{\alpha,w} \left.\frac{\partial y^\gamma_\alpha}{\partial r}\right|_w . \tag{2.22}$$

We assume that Henry's law holds. This means that there is a simple linear relation between the concentration of dissolved air and its partial pressure in the gas phase (Sander 2015):

$$p^G_{Air,w} = x^L_{Air,w} H_m, \tag{2.23}$$

where H_m is the Henry coefficient. We formulate (2.23) for the mass fraction $y^L_{Air,w}$, which is detailed in § A.3.

Together with the ideal gas law (2.4), $p^G = \rho^G_{m,w} \mathcal{R}_{m,w} T^G_w$ and the complement (2.1), $\sum_{\alpha=1}^{N_S} y^G_{\alpha,w} = 1$ and $\sum_{\alpha=1}^{N_S} y^L_{\alpha,w} = 1$ a closed boundary equation set for the evaluation of the dependent variables at the bubble wall has been obtained.

2.4. *Initial conditions*

The bubble is initialized (subscript 0) in mechanical and thermal equilibrium in terms of R_0, $T^G_0 = T^L_0 = T_0$ and $p^L_{\infty,0}$. The mass fractions $y^G_{\alpha,0}$ and $y^L_{\alpha,0}$ are prescribed homogeneously, according to the phase equilibrium equation (2.19) and Henry's law (2.23), together with (2.1). The initial bubble pressure p^G_0 is evaluated by (2.17) by setting $p^L_{w,0} = p^L_{\infty,0}$, $\dot{R} = 0$, $\ddot{R} = 0$, $\dot{m}''_0 = 0$ and $\ddot{m}''_0 = 0$. It should be noted that by (2.23), $y^L_{Air,0}$ is evaluated by p^G_0 and thus depends on R_0. This initialization might deviate from real situations where the liquid is usually saturated with air at ambient pressure, and not at bubble pressure, which should be considered when comparisons with experimental data are planned. After initialization, the bubble motion is driven by the temporal evolution of p^L_∞, which will be specified for the particular test cases in § 4.

2.5. *Thermophysical properties*

For pure fluids, thermophysical properties – e.g. thermal conductivity, heat capacity, latent heat, saturation pressure and diffusion coefficients – depend on temperature and pressure. In fluid mixtures, they depend additionally on the local mixture composition. We present a detailed calculus of properties in § A.4. Here, we discuss briefly their dependence on T and p.

In anticipation of the results presented in § 4, this dependence of properties on T and p has been assessed by preliminary simulations. On the one hand, properties have been evaluated with their full T and p dependence. On the other hand, properties have been evaluated at a fixed reference state, which we chose to be the initial temperature and pressure. Based on a comparison of both variants, we assess the T and p dependence of each property. We do not present the details here, but summarize that while the T dependence of the diffusion coefficients in the gas phase D^G_α (see (A22) and (A23)) is insignificant, its pressure dependence affects the results significantly. For example, the mass flux at the bubble interface rises by more than 100 % for a rapid pressure drop when D^G_α is evaluated at the initial pressure instead of the instantaneous value of p^G.

Also, the temperature dependence of vapour saturation pressure p_m^{Sat} (A27) is important, albeit to a lesser extent. The T and p dependence of all other properties can be neglected. Of course, this assessment of property impact is not general but certainly confined to the particular test cases under consideration. A more in-depth analysis is considered out of scope here. For convenience, all results presented in § 4 have been obtained with full T and p dependence of properties, and details of their evaluation are provided in § A.4.

Moreover, we consider the dependence of thermophysical properties on local mixture composition as crucial for alkane mixtures. While in this study we accept the uncertainties on mixture composition that have been introduced by the simple Raoult's law as discussed above, we introduce an even more crude simplification by comparison with a pseudo-fuel whose components cannot segregate. For the pseudo-fuel, properties are evaluated at a reference mixture state in terms of the initial mixture composition. Details of this simplified mathematical model are presented in § 2.6.2.

2.6. *Variants of the mathematical model*

2.6.1. *Discrete fuel model (full model)*

In the model presented so far, the full transport processes have been considered. A discrete mixture of heptane and dodecane has been described by different mass fractions y^{γ}_{Hep} and y^{γ}_{Dod} for both the liquid ($\gamma = L$) and gas ($\gamma = G$) phases. By solving mass fraction equations for each alkane in terms of (2.3), the transport of each individual species is considered so that interdiffusion of both alkanes is enabled, and the fuel may segregate locally. This segregation-prone two-component heptane/dodecane fuel is termed discrete fuel in the following. In the next subsubsection, we introduce a simplification to the discrete fuel model by lumping the fuel species together into one single-component pseudo-fuel.

2.6.2. *Pseudo-fuel model (simplified model)*

It is interesting to see how bubble dynamics changes when we define a bulk fuel with an invariant mixture composition. In a simplified version of the discrete fuel model, a single-component fuel is introduced with a fuel mass fraction y^{γ}_{Fuel}. This is initialized by $y^{\gamma}_{Fuel,0} = y^{\gamma}_{Hep,0} + y^{\gamma}_{Dod,0}$, in which $y^{\gamma}_{Hep,0}$ and $y^{\gamma}_{Dod,0}$ correspond to the initial mixture composition of heptane and dodecane. This surrogate single-component fuel is termed pseudo-fuel in the following. Per definition, the pseudo-fuel has the same initial composition as the discrete counterpart, but interdiffusion of the alkanes is disabled, and the mixture cannot segregate, which means that its composition is invariable for both the gaseous in-bubble ($\gamma = G$) and the surrounding liquid ($\gamma = L$) phases. For the pseudo-fuel, all mixing rules for the property evaluation specified in § A.4 hold, but in contrast to the discrete fuel, they are evaluated by the invariable, initial mixture state of the pseudo-fuel. It is important to note that as in the liquid phase, also the invariable gaseous phase of the pseudo-fuel model corresponds to the initial composition of the discrete counterpart. Thus the initial bubble content in terms of the fuel/air mixture ratio is the same for both discrete fuel and pseudo-fuel mixtures. The governing equations hardly change compared to the discrete fuel model, with one exception: for the discrete fuel, mass fraction equations (2.3) are solved for each discrete species, i.e. y^{γ}_{Hep}, y^{γ}_{Dod} and y^{γ}_{Air}. For the pseudo-fuel, only one fuel species exists, so the solution of (2.3) is restricted to y^{γ}_{Fuel} and y^{γ}_{Air}.

2.7. *Note on mass conservation and species complement*

In case of only two species ($N_S = 2$), (2.1) and (2.2) are fulfilled readily when we solve (2.3) for both species, assuming equality of binary diffusion coefficients D_α^γ. In fact, by summing (2.3), we obtain (2.2). We encounter a two-species system – e.g. for pure heptane or pure dodecane with air – and this is also the case for the single-component pseudo-fuel (introduced in the preceding subsection) with air. In the case of discrete heptane/dodecane mixtures with air, however, we face a three-species system ($N_S = 3$). The diffusion coefficients D_α^L (see (A17)) and D_α^G (see (A22)) correspond to equivalent diffusion of species α into the rest of the mixture (Hirschfelder, Curtiss & Byrd 1969). Thus generally, summing (2.3) may not result in (2.2), and mass conservation may not be fulfilled. Furthermore, solving (2.3) for all three species may violate the species complement (2.1). In preliminary simulations, we have tested different means to enforce both mass conservation and species complement, and how we calculate mixture density ρ_m^γ and mass fraction y_α^γ of species α. Details are provided in § 2 of the supplementary material. Here, we summarize that exact fulfilment of mass conservation by (2.2) has little effect on the results. This means that regardless how we calculate ρ_m^γ, the effect on the results in § 4 is insignificant. Therefore, gas mixture density ρ_m^G is evaluated by the ideal gas law (2.4). Liquid mixture density ρ_m^L is also evaluated by an equation of state in terms of (A8). We have verified that by this procedure, (2.2) is fulfilled approximately. We solve (2.3) for only two of three species and ensure species complement by solving (2.1) for the remaining species.

3. Simulation method

The governing equations constitute a coupled nonlinear set of partial differential equations. The numerical scheme and the solution procedure have been presented in detail by Bermudez-Graterol *et al.* (2021) for a water–air system. Their extension to alkane mixtures is straightforward, so the simulation method is summarized only briefly here.

The bubble interior and its surrounding liquid are discretized in the radial direction by computational nodes with a grid clustering at the bubble wall to resolve the gradients. In preliminary simulations, an extent of the liquid domain that corresponds to $r/R = 5$ has been found to be adequate for each test case considered. Computational cells are constructed between nodes. A staggered variable arrangement is employed, which means that the velocity is stored at node locations, and all other variables are stored at cell centre locations. Ghost cells are introduced to store the boundary values at the bubble centre, at the bubble interface and in the liquid far field. The bubble wall moves with the velocity $\dot{R}$, and the governing equations are solved by an arbitrary Lagrangian–Eulerian (ALE) method according to e.g. Hirt, Amsden & Cook (1997), on a grid that moves with the bubble wall.

The mass fraction equations are solved in their conservative form by a finite volume discretization and a central scheme, which means a linear interpolation of cell centre values to node locations. For the other equations, a finite difference scheme is used, where the spatial derivatives are approximated by central differences. All integration operations, e.g. in (2.5)–(2.7), are performed by the midpoint rule. By this combined central finite volume/finite difference scheme, we have obtained a simple and robust second-order-accurate scheme. An evaluation of the magnitude of the Péclet number Pe^{num} has been performed, since large values of Pe^{num} may promote artificial wiggles in the numerical solution. For any simulation result presented in § 4, Pe^{num} amounts to less than

0.01 at any location within the bubble and at any time instant. Regarding the liquid side, Pe^{num} is even significantly smaller close to the bubble wall due to a very fine grid, but may grow up to about 10^2 towards the liquid far field for some cases and time instants. In spite of this rather large value, a careful inspection of the numerical solution field did not reveal any wiggles, since far away from the bubble wall, gradients of any flow variable vanish and the solution is homogeneous.

Time integration is performed by an implicit Crank–Nicolson scheme (Crank & Nicolson 1996). Time steps correspond to a maximum Courant–Friedrichs–Lewy (CFL) number of about 100, and convergence within each time step is achieved when the dimensionless residuals of each equation have dropped below 1×10^{-8}.

At the bubble wall, 12 unknown boundary quantities in terms T_w^G, T_w^L, $y_{\alpha,w}^L$, $y_{\alpha,w}^G$, $\dot{m}_\alpha''$ and $\rho_{m,w}^G$ need to be evaluated, with $\alpha = Hep$, Dod or Air. Heat balance (2.20), mass balance (2.22), Henry's law (A7) and the ideal gas law (2.4), together with (2.18) and (A6), are solved. These 12 equations constitute a closed nonlinear equation set that is solved by a Newton method.

The computer program *sibub* (= *si*ngle *bub*ble dynamics) is coded by Fortran 90 and run on a conventional Linux workstation. Program *sibub* has been validated thoroughly for water in our preceding study (Bermudez-Graterol *et al.* 2021), which is particularly important since no measurement data on bubble dynamics in binary alkane mixtures are available.

4. Results

4.1. *Bubble oscillation after a rapid pressure drop*

4.1.1. *Case description*

A bubble with $R_0 = 100$ µm at $T_0 = 293.15$ K is initialized in a liquid fuel mixture with mass fraction ratio 25 % heptane and 75 % dodecane, referred to as a 25/75 % mixture in what follows. It is important to note that this mixture ratio refers to the liquid fuel mixture outside the bubble, while the mixture ratio of the gaseous phase within the bubble results from the equilibrium initialization. Details on the fuel mixture initialization are provided in § 3 of the supplementary material. The bubble is exposed to a rapid pressure drop from $p_\infty^L = 10^5$ to 10^4 Pa within 100 µs, which corresponds to a drop rate of $\mathrm{d}p_\infty^L/\mathrm{d}t = 9 \times 10^8$ Pa s^{-1}. The final pressure level is well above the saturation pressure of any mixture component, so no excessive growth by phase change occurs, but the bubble is rather excited to oscillate. A computational grid with $n^G = 200$ and $n^L = 800$ nodes within and outside the bubble, respectively, with a strong node clustering at the bubble wall, is used, which has been ensured to yield grid-independent results in preliminary simulation runs.

For an oscillating gas bubble, Prosperetti (1991) used the ratio of the thermal penetration length to the initial bubble radius to assess the effect of heat transfer on bubble motion. This ratio corresponds to the inverse Péclet number Pe^G (not to be confused with Pe^{num} in § 3, which characterizes the ratio of convective to diffusive flux in a numerical scheme). Here, Pe^G is equivalent to the ratio of thermal diffusion time scale to bubble motion, i.e. dynamic time scale. For small values of Pe^G, the bubble temperature variation is insignificant, while for large values, most of the gas in the bubble is thermally insulated from the liquid. Fuster & Montel (2015) and Bergamasco & Fuster (2017) analysed the influence of mass transfer on the dynamic response of oscillating bubbles. We adopt their evaluation of dynamic and thermal diffusion time scale in terms of $t_{dyn} = 1/f$ and $t_{diff} = R_0^2/D_T^G$, with thermal diffusivity $D_T^G = \lambda_m^G/(\rho_m^G c_{p,m}^G)$. In the studies by Prosperetti

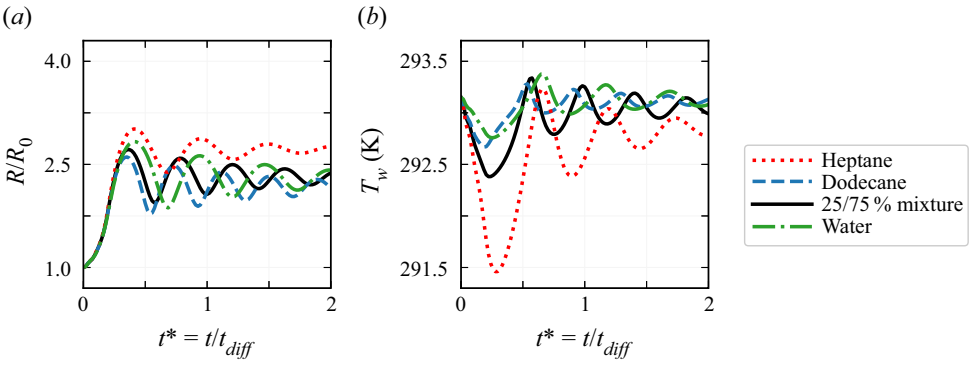

Figure 1. Temporal progression of (*a*) bubble radius and (*b*) wall temperature, for different fluids. The 25/75 % heptane/dodecane mixture corresponds to the discrete model according to § 2.6.1.

(1991), Fuster & Montel (2015) and Bergamasco & Fuster (2017), bubble oscillation due to an enforcing sinusoidal pressure wave with an angular frequency ω has been investigated. Since we excite our bubble with a one-time pressure drop, the frequency f is evaluated simply by the bubble response frequency. We obtain $Pe^G = 2$, so according to Bergamasco & Fuster (2017), thermal effects will be relevant. When we evaluate Pe^G with the mass diffusion coefficient D^G_α according to (A22), instead of the thermal diffusivity D^G_T, and average over all three species and over time, we obtain $Pe^G = 0.6$, which is of the same order of magnitude.

4.1.2. *Discrete fuel model results*

In figure 1(*a*), the initial phase of the bubble radius oscillation is depicted. The time is related to the thermal diffusion time scale in terms of $t^* = t/t_{diff}$, where $t_{diff} = 5 \times 10^{-4}$ s for the discrete fuel mixture. As reference, bubbles in pure heptane, pure dodecane and water are considered. Water properties are adopted from Bermudez-Graterol *et al.* (2021), and the time axis of any fluid is scaled with the same value $t_{diff} = 5 \times 10^{-4}$ s for convenience. The oscillation is damped by thermal effects, while viscous damping essentially plays no role. The damping effect is most pronounced for pure heptane, which is traced back to a strong initial liquid temperature drop close to the bubble wall, illustrated in figure 1(*b*). Bubble oscillation is affected by alternating heat and mass flux over the bubble wall. Similar to what was observed for rectified diffusion processes (Hsieh & Plesset 1961; Crum 1984), a net heat and mass flux into the bubble arises. While the initial content of any bubble is dominated by air, evaporation changes the bubble content. This is most pronounced for the heptane bubble due to high volatility of heptane, so that its net vapour mass flux is largest. At $t^* = 2$, the heptane bubble contains most vapour, and its final radius is thus greater than that of the others.

The discrete 25/75 % mixture corresponds to a two-component fuel that is prone to segregation. A more thorough look at the 25/75 % mixture reveals that mass transfer of the different species through the bubble wall is considerably different. According to figure 2(*a*), the entire mass flow is dominated by $\dot{m}_{Hep}$, while $\dot{m}_{Dod}$ and $\dot{m}_{Air}$ are approximately two orders of magnitude lower – note the augmented illustration of $\dot{m}_{Dod}$ and $\dot{m}_{Air}$ by a factor of 50 in figure 2(*a*). The small mass flow of air illustrates that air release is a relatively slow process, compared to fuel component transfer by evaporation. The small dodecane mass flow comes along with its small content within the bubble:

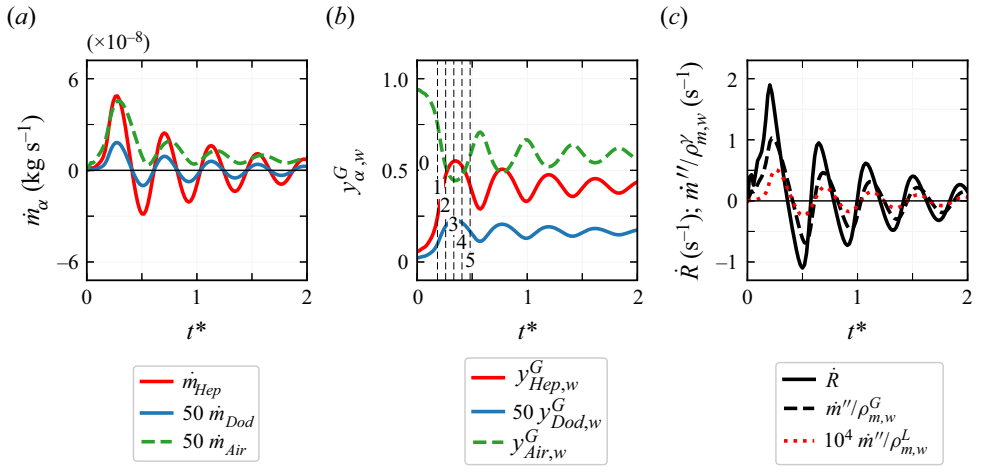

Figure 2. Temporal progression of (*a*) mass flows through the bubble wall, (*b*) mass fractions within the bubble at the wall, and (*c*) velocity components at the bubble wall according to (2.8) and (2.13), for a discrete 25/75 % heptane/dodecane mixture.

in figure 2(*b*), the mass fraction at the gaseous side of the bubble wall $y^G_{\alpha,w}$ is presented, where $\alpha = Hep, Dod$ or Air. Heptane and air are present predominantly within the bubble, while dodecane represents only a minor species – note again the augmented illustration of $y^G_{Dod,w}$. The low amount of dodecane at the inner bubble wall is associated with its low volatility in terms of low vapour saturation pressure $p^{Sat}_{Dod}|_{T^L_W}$, which is about two orders of magnitude lower than that of heptane, and according to the saturation interface condition in terms of (A6), $y^G_{Dod,w} \ll y^G_{Hep,w}$ arises. On the other hand, $y^G_{Air,w}$ is even slightly bigger than $y^G_{Hep,w}$ for most instants of time, which means that the amount of air within the bubble is of the same order as the amount of heptane. On the liquid side of the bubble wall, the amount of dissolved air in terms of $y^L_{Air,w}$ (not shown) has dropped from its initial value to a level within a range of merely 10^{-5} to 10^{-4}, and is thus low. On the other hand, the amount of $y^G_{Air,w}$ within the bubble is in the range 0.5 to 0.7 and thus much bigger than the liquid, which is governed by Henry's law in terms of (A7).

In figure 2(*c*), the bubble wall velocity contributions in (2.8) and (2.13) are shown. Since $\dot{m}''/\rho^L_{m,w} \ll \dot{R}$ (note the strongly augmented illustration of $\dot{m}''/\rho^L_{m,w}$), mass transfer does not immediately control the dynamic response of the bubble via (2.12), which reduces to the classical Rayleigh–Plesset equation, when mass flux is neglected. However, the species mass flux $\dot{m}''_\alpha$ enters also the transport equations (2.8), (2.20) and (2.22), and therefore affects the bubble content. This is underlined by $\dot{m}''/\rho^G_{m,w}$ in figure 2(*c*), which has the same order of magnitude as $\dot{R}$. Therefore, bubble response is affected not by mass flow terms in the Rayleigh–Plesset equation (2.12), but rather via the effect of mass transfer on the bubble content, as already pointed out by Bermudez-Graterol *et al.* (2021) for an air–water system. Thus staggered mass flow rates $\dot{m}_\alpha$ of the individual mixture components (figure 2*a*) govern the bubble content, which has been illustrated by the distinctive mass fractions in figure 2(*b*).

The fact that the mass flows of heptane and dodecane are clearly different indicates a local mixture segregation of the fuel. In figure 3, the temporal progression of

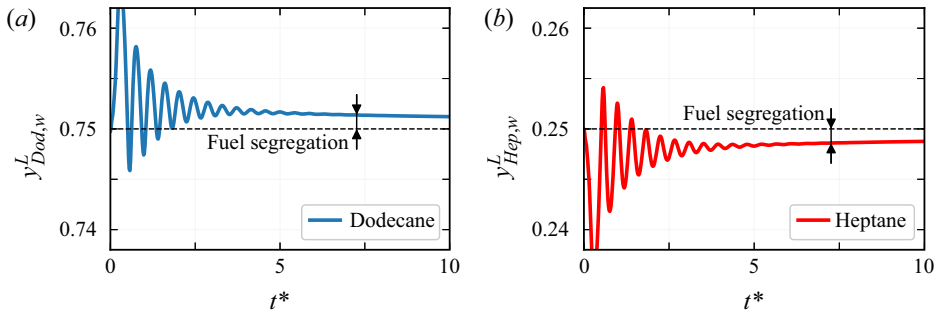

Figure 3. Temporal progression of (*a*) dodecane and (*b*) heptane liquid mass fractions at the bubble wall for a discrete 25/75 % heptane/dodecane mixture.

the wall-adjacent liquid mass fraction of both fuel components is illustrated. In fact, particularly for early instants of time, $y^L_{Hep,w}$ and $y^L_{Dod,w}$ deviate significantly from their initial values of 25 % and 75 %, respectively. This mixture segregation is quite dynamic at the beginning, and after the oscillation has abated, a rather small deviation from the initial mixture ratio 25/75 % remains, which corresponds to a new equilibrium state. The local de-mixing is illustrated in more detail by the radial distribution of mass fractions of each species, which are evaluated at selected instants of time, marked by the labels 0–5 in figure 2(*b*). Instants 0–3 correspond to the initial expansion period, and instants 4 and 5 to the subsequent compression period of the bubble motion. For these instants of time, radial profiles of y^L_α are plotted in figure 4 over the dimensionless radial coordinate r/R, where $r/R = 1$ and $r/R > 1$ corresponds to the bubble wall and the surrounding liquid, respectively. Here, we focus on the discussion of the liquid side of the bubble, while the discussion of the bubble interior is left to § 4.1 of the supplementary material.

Clearly, a boundary layer is discernible on the liquid side for any species. In figure 4(*c*), y^L_{Air} shows a continuous drop from instant 0 to instant 5. According to the positive value of $\dot{m}_{Air}$ throughout figure 2(*a*), air is desorbed continuously from the surrounding liquid into the gaseous phase of the bubble. For compression instants 4 and 5, the drop of y^L_{Air} stagnates and even slightly attenuates, which is, however, restricted to the immediate wall proximity, as depicted in close-up A in figure 4(*c*). Both liquid fuel components y^L_{Hep} and y^L_{Dod} show a more pronounced trend reversal between instant 3 and 4, and the spatial gradient clearly changes its sign, according to figures 4(*a*,*b*). It is interesting to note that in contrast to the bubble interior, the trend of heptane and dodecane content is opposite in the liquid: during instants 0–3, y^L_{Hep} shows a positive and y^L_{Dod} a negative spatial gradient in the near-bubble liquid. Therefore, heptane gets leaner and dodecane richer in the proximity of the bubble interface. Between instants 3 and 4, this trend reverses for both fuel components. Thus there is a clear local segregation of the liquid fuel composition, which is confined to the bubble interface proximity. It is also interesting to note that although the spatial gradients of $y^L_{Hep,w}$ and $y^L_{Dod,w}$ are opposite at any instant of time, $\dot{m}_{Hep}$ and $\dot{m}_{Dod}$ are not, according to figure 2(*a*), which means that fuel components invariably flow in the same direction. In figure 5(*a*), the entire species mass flow $\dot{m}_\alpha$ is illustrated by its convective and diffusive parts, $\dot{m}_{\alpha,conv} = -4\pi R^2 \rho^L_{m,w} y^L_{\alpha,w}(u^L_w - \dot{R})$ and $\dot{m}_{\alpha,diff} = 4\pi R^2 \rho^L_{m,w} D^L_{\alpha,w}(\partial y^L_\alpha/\partial r)|_w$, according to (2.21). Since $\dot{m}_{Hep,conv}$ and $\dot{m}_{Dod,conv}$ are immediately associated with the same relative velocity in terms of $u^L_w - \dot{R}$, they inherently flow in the same direction. For heptane, according to figure 5(*a*)(i), the

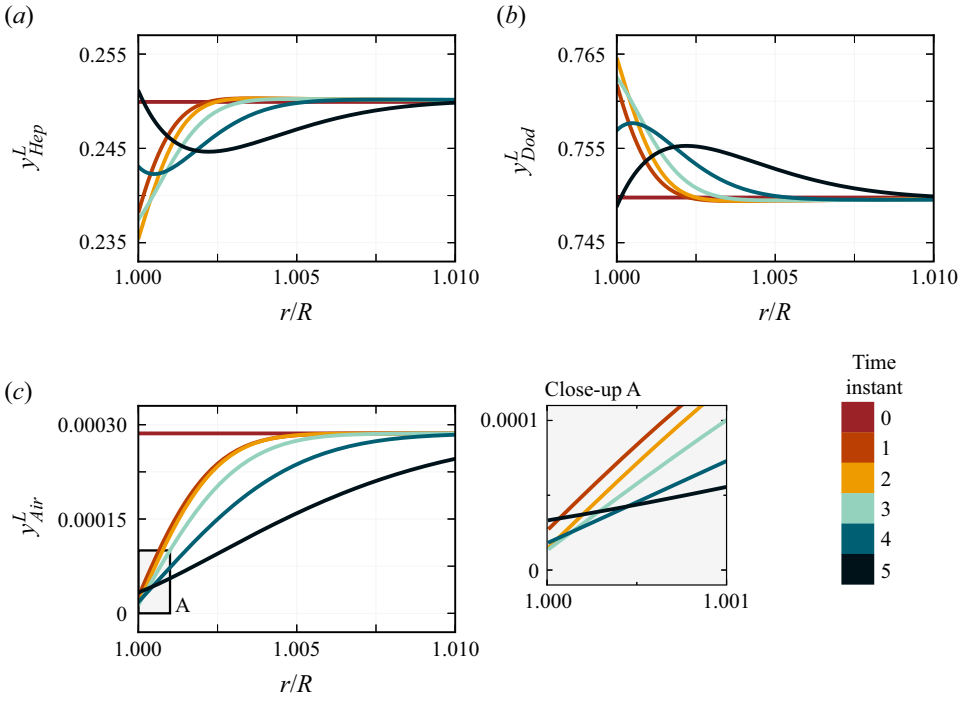

Figure 4. Radial distribution of species around the bubble for a discrete 25/75 % heptane/dodecane mixture. (*a*) Heptane, (*b*) dodecane and (*c*) air mass fraction within liquid. Time instants 0–5 are marked in figure 2(*b*).

convective and diffusive parts have the same sign and thus add up to the entire mass flow $\dot{m}_{Hep}$. A different situation becomes apparent for dodecane, according to figure 5(*a*)(ii): from the opposed y^L_{Dod} gradient due to interdiffusion of both fuel species, $\dot{m}_{Dod,diff}$ is opposed to its heptane counterpart, and $\dot{m}_{Dod,conv}$ and $\dot{m}_{Dod,diff}$ cancel out essentially, leading to a level of $\dot{m}_{Dod}$ that is two orders of magnitude lower than $\dot{m}_{Hep}$ – note again the augmented illustration of $\dot{m}_{Dod}$ by a factor of 50 in figure 5(*a*)(ii).

The fact that $\dot{m}_{Dod}$ invariably flows in the same direction as $\dot{m}_{Hep}$ is not at all confined to the particular 25/75 % mixture ratio. To demonstrate this, in figures 5(*b*,*c*), the same illustration of convective and diffusive contribution is presented for different liquid mixture ratios. In figure 5(*b*), a rich heptane mixture in terms of a 99/01 % heptane/dodecane ratio, and in figure 5(*c*), a lean heptane mixture in terms of a 0.3/99.7 % heptane/dodecane ratio, are shown. The plots are augmented where applicable for clarity of illustration. For the heptane-rich 99/01 % mixture, the $\dot{m}_{Dod}$ level is even significantly lower than for the 25/75 % mixture. With rising dodecane percentage up to the 0.3/99.7 % heptane/dodecane mixture ratio, the entire dodecane mass flow $\dot{m}_{Dod}$ approaches the level of $\dot{m}_{Hep}$, according to figure 5(*c*). It is interesting to note that in spite of the strongly different levels of $\dot{m}_{Hep}$ and $\dot{m}_{Dod}$, $\dot{m}_{Hep,conv}$ and $\dot{m}_{Hep,diff}$ are always oriented in the same direction, for any liquid mixture ratio. On the other hand, $\dot{m}_{Dod,conv}$ and $\dot{m}_{Dod,diff}$ are always oriented in opposite directions, for any liquid mixture ratio. To pursue this observation, we performed simulations with several further binary mixtures of different alkanes, from the very high-volatile hexane (C6H14) to the very low-volatile hexadecane (C16H34). We do not present the results in detail here, but rather summarize that irrespective of the alkane pair and the liquid mixture ratio, $\dot{m}_{conv}$ and $\dot{m}_{diff}$ are always

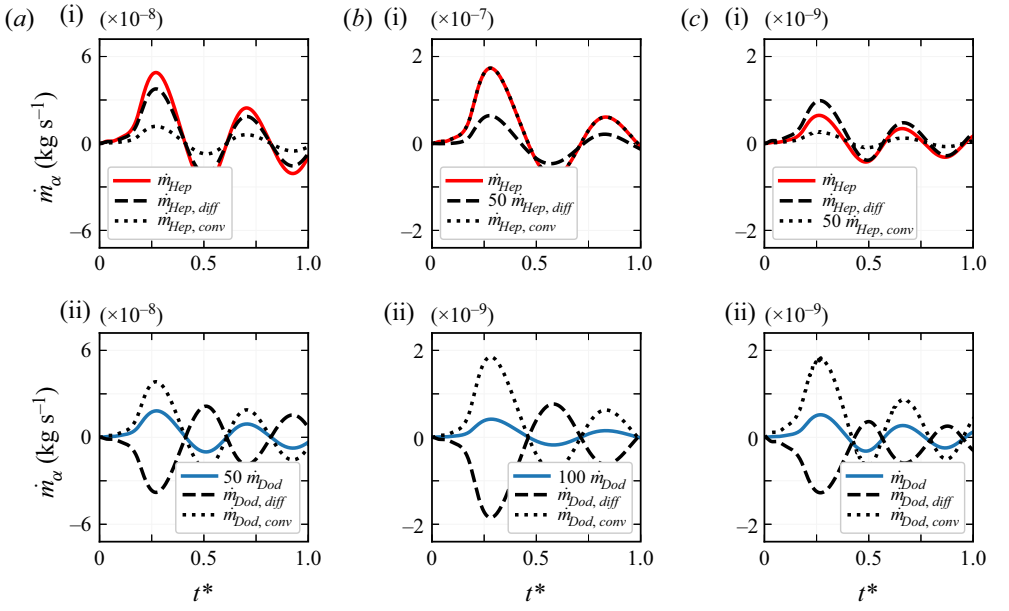

Figure 5. Convective and diffusive contributions to the (i) heptane and (ii) dodecane mass flows of a discrete heptane/dodecane mixture at (*a*) 25/75 %, (*b*) 99/01 %, and (*c*) 0.3/99.7 %.

oriented in the same direction for the higher-volatile alkane. On the other hand, $\dot{m}_{conv}$ and $\dot{m}_{diff}$ always flow in opposite directions for the lower-volatile alkane. In other words, the low-volatile component is displaced by the high-volatile component, by means of diffusion. Thus our observation on the particular high-volatile heptane and low-volatile dodecane pair does not seem to be specific for these two alkanes but seems to hold for any binary mixture of alkanes with different volatilities. From here on, we proceed again with the 25/75 % heptane/dodecane pair.

4.1.3. *Pseudo-fuel model results*

So far, we have studied a discrete mixture of heptane and dodecane by the full model according to § 2.6.1. Now we apply the pseudo-fuel model according to § 2.6.2. Detailed results are depicted in § 4.2 of the supplementary material, where we compare radial profiles of y^G_{Fuel} and y^L_{Fuel} for both fuel models. Here, we summarize that for example, y^G_{Fuel} and y^L_{Fuel} show a dispensable deviation between pseudo-fuel and discrete fuel mixture. The same holds for other flow variables, e.g. velocity and temperature. The difference between discrete fuel and pseudo-fuel is particularly not discernible in the motion of the bubble wall, so local fuel segregation does not affect bubble dynamics. In what follows, we demonstrate that this observation is highly test-case-specific.

4.2. *Bubble growth in superheated liquid*

4.2.1. *Case description*

Until this point, we have investigated a pressure drop with a final pressure level above the saturation pressure, so that no continuous growth occurred, but the bubble was rather excited to oscillate. Now a superheated liquid with a constant superheat level ΔT_{SH} is

considered, which means that the pressure level is below the vapour saturation pressure, so that the bubble grows continuously. The superheat level is immediately associated with a pressure difference $\Delta p_{Tension}$ by the Clausius–Clapeyron relation, which can be approximated as (Brennen 1995)

$$\frac{\Delta p_{Tension}}{\Delta T_{SH}} = \frac{\rho_{vap}^{G} L_m}{T^L}, \tag{4.1}$$

where ρ_{vap}^{G} is the vapour density at saturation pressure conditions. The early stage of bubble growth is limited by momentum interaction between the liquid and the bubble, and bubble growth rate approaches the asymptotic limit $\dot{R} \sim$ const. (Plesset & Prosperetti 1977):

$$\dot{R} = \sqrt{\frac{2}{3}\frac{\Delta p_{Tension}}{\rho_m^L}}. \tag{4.2}$$

As the bubble grows, heat transfer becomes more important until it dominates the growth rate, which is then bounded by the heat diffusion in the liquid, and the bubble growth rate approaches the asymptotic limit $\dot{R} \sim t^{-1/2}$ (Forster & Zuber 1954; Plesset & Zwick 1954):

$$\dot{R} = \frac{\Delta T_{SH}\, \rho_m^L c_m^L}{\rho_{vap}^{G} L_m}\sqrt{\frac{3\alpha_m^L}{\pi t}}. \tag{4.3}$$

While for an oscillating bubble the Péclet number Pe^G has been used e.g. by Fuster & Montel (2015) and Bergamasco & Fuster (2017) to discuss thermal effects, for a continuously growing bubble, rather the time when thermal effects become important may be considered. Mikic, Rohsenow & Griffith (1970) performed *ad hoc* interpolations between both limiting solutions. They introduced a dimensionless characteristic time t^+, where for $t^+ \ll 1$ and $t^+ \gg 1$, respectively, the limiting solutions in terms of (4.2) and (4.3) are retained. Prosperetti & Plesset (1978) proposed an approximation similar to that of Mikic *et al.* (1970), albeit putting it on a firm theoretical basis. In their more recent study, Chernov *et al.* (2020) introduced a characteristic time that is convenient for the analysis of the transition stage of bubble growth. In terms of the first critical time t_{c1}, Brennen (1995) proposed an instant of time at which inertia-dominated growth transitions to thermally dominated growth:

$$t_{c1} = \Delta p_{Tension}/(\rho_m^L \Sigma^2), \tag{4.4}$$

with the thermodynamic parameter

$$\Sigma = \frac{[L_m \rho_{vap}^{G}]^2}{T_0^L \sqrt{(\rho_m^L)^3 c_m^L \lambda_m^L}}, \tag{4.5}$$

where t_{c1}, according to (4.4), is obtained simply by equating (4.2) and (4.3) (Prosperetti 2017).

In the simulation, the initial bubble radius R_0 corresponds to the mechanical equilibrium of a vapour bubble, as has been proposed by e.g. Prosperetti & Plesset (1978), Lee & Merte

Symbol	Unit	Case 1	Case 2	Case 3	Case 4	Case 5
T_0^L	K	374.6	375.3	376.3	377.7	378.5
R_0	μm	22.0	15.6	10.2	7.5	5.2
ΔT_{SH}	K	1.4	2.1	3.1	4.5	5.3
$\Delta p_{Tension}$	Pa	5963	8901	13 099	18 975	22 333
t_{c1}^*	–	0.14	0.2	0.3	0.44	0.5

Table 1. Initial and boundary conditions for bubble growth in superheated water at 373.15K.

(1996) and Robinson & Judd (2004):

$$R_0 = \frac{2\sigma_m}{\Delta p_{Tension}}. \tag{4.6}$$

Since we prefer to input a driving pressure rather than a driving temperature in the simulation, ΔT_{SH} is reformulated to a pressure difference in terms of the tension $\Delta p_{Tension}$. The liquid pressure drops from its initial value $p_m^{Sat}|_{T_0^L}$ instantaneously to its final value p_∞^L, where the pressure difference $\Delta p_{Tension} = p_m^{Sat}|_{T_0^L} - p_\infty^L$ corresponds to the nominally prescribed superheat level ΔT_{SH}. Note that by using a temperature regression in terms of e.g. (A27), this procedure is more accurate than using a Clausius–Clapeyron approximation according to (4.1). By a large drop rate of 10^9 Pa s^{-1}, for any superheat level considered in the study, the results can be assumed to be drop-rate-independent (Bermudez-Graterol *et al.* 2021).

In § 4.2.2, we present a validation of the simulation on experimental water data, before we proceed in §§ 4.2.3–4.2.5 with alkane mixtures.

4.2.2. *Water at 373.15 K*

In the experiments by Dergarabedian (1953), the tension in the liquid surrounding the bubble is imposed by superheating the liquid to 373.15 K + ΔT_{SH} at atmospheric pressure. Boundary conditions of the test case by Dergarabedian (1953) are listed in table 1 for different superheat levels. In figure 6, measurement data in terms of the bubble growth rate versus time are presented together with the asymptotic limit by Plesset & Zwick (1954) i.e. (4.3). We choose a dimensionless representation of $(\dot{R}/R_0)t_{diff}$ in dependence on the dimensionless time $t^* = t/t_{diff}$. As in § 4.1, we use the thermal diffusion time t_{diff} as reference time. For convenience, the same $t_{diff} = 5$ μs of case 3 is used to scale the results of the other cases, 1, 2, 4 and 5, and t_{c1}^* is also listed in table 1. Compared to the abscissa scale of figure 6 spanning the range up to $t^* \approx 10^4$, t_{c1}^* is very small for any value of ΔT_{SH}, so bubble growth should be thermally controlled in the time range considered, except for a very short initial inertia-driven period. The double logarithmic scale reveals that the data approach the asymptotic limit $\dot{R} \sim t^{-1/2}$, which corresponds to the approximation by Plesset & Zwick (1954) and in fact clearly indicates a thermally controlled bubble growth rate.

In the simulation, we input a driving pressure, so that initial pressure drops from $p_{H_2O}^{Sat}|_{T_0^L}$ to atmospheric pressure $p_\infty^L = 1.014 \times 10^5$Pa with saturation temperature $T_{H_2O}^{Sat}|_{p_\infty^L} = 373.15$K. Thus superheat amounts to $\Delta T_{SH} = T_0^L - T_{H_2O}^{Sat}|_{p_\infty^L}$. The resulting values of $\Delta p_{Tension}$ are listed in table 1. Simulation results have been obtained on a grid with $n^G =$

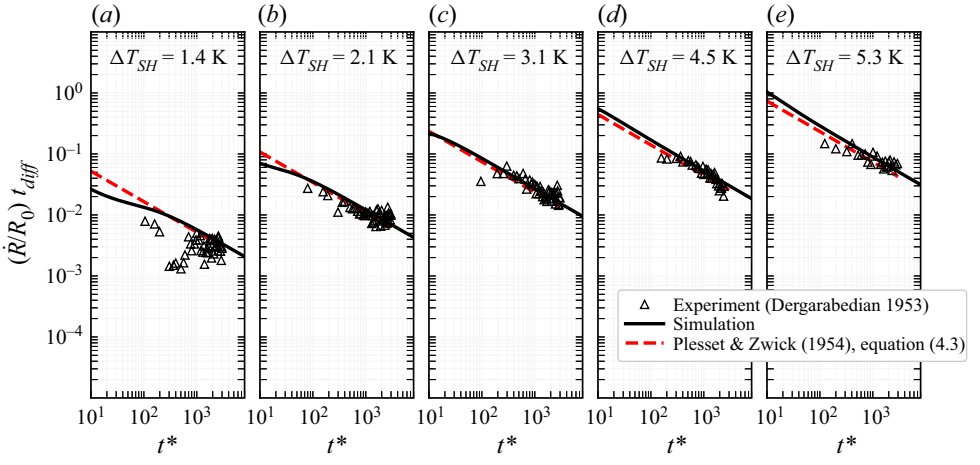

Figure 6. Non-dimensional representation of bubble growth in terms of $\dot{R}$ versus time for water at different superheat levels, corresponding to cases 1–5 in (*a*)–(*e*).

100 and $n^L = 400$ and a strong node clustering towards the bubble wall. In preliminary simulations with a variation of the spatial resolution, grid independence of the results has been assured. The simulation results are also presented in figure 6. In the experiment (Dergarabedian 1953), the time uncertainty when the bubble starts to grow amounts to about 1 ms, which corresponds to $t^* \approx 10^2$, and the data show considerable scatter. The simulation results are well within the scatter of measurement data, and regarding the considerable measurement uncertainty, a good match is obtained. In particular, the simulation results well approach the asymptotic limit by Plesset & Zwick (1954). Further comparisons to experimental data by Lien (1969) and Board & Duffey (1971), as well as simulation results by Robinson & Judd (2004), also reveal a very good match. These results are reported in § 5 of the supplementary material.

4.2.3. *Binary heptane/dodecane mixtures at 303.15 K: temporal bubble growth for discrete fuel and pseudo-fuel*

For alkane investigations, we choose initial temperature $T_0^L = 303.15$ K. For a constant superheat level $\Delta T_{SH} = 10$ K, we vary the liquid mixture ratio in the range from pure heptane to dodecane-rich mixtures. Since fluid properties vary with the mixture ratio, $\Delta p_{Tension}$, t_{c1} and R_0 also vary, according to (4.1), (4.4) and (4.6); R_0 varies in the range 12–70 µm, from pure heptane to a 01/99 % heptane/dodecane mixture. For convenience, a uniform initial value $R_0 = 100$ µm is specified for any mixture ratio, which is well above the equilibrium radius of even the most dodecane-rich mixture considered. The tension $\Delta p_{Tension}$ rises for a more heptane-rich mixture percentage, according to figure 7. As shown in the same figure, t_{c1} drops considerably with rising heptane percentage, so it can be assumed that thermal effects set in earlier for heptane-rich mixtures.

In figure 8, the time progression of $\dot{R}$ is presented for selected fuel mixture ratios and both discrete fuel and pseudo-fuel, ranging from 100/0 % (pure heptane) to a 01/99 % heptane/dodecane mixture. Again, results are rendered dimensionless by t_{diff}. We have evaluated $t_{diff} = 40$ ms for the 05/95 % heptane/dodecane mixture, and use this value for any mixture ratio for convenience. Simulations have been run for a very long physical time range up to $t^* = t/t_{diff} \approx 10^6$, which is certainly beyond technical relevance. On the

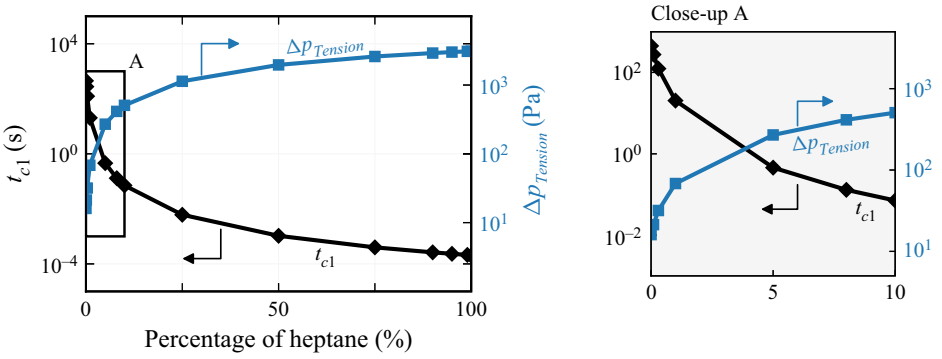

Figure 7. First critical time t_{c1} according to (4.4) (left abscissa) and tension $\Delta p_{Tension}$ (right abscissa) in dependence on heptane percentage.

other hand, these long-term runs reveal that for any mixture ratio and for both discrete fuel and pseudo-fuel models, the growth rate approaches the asymptotic limit $\dot{R} \sim t^{-1/2}$. This asymptotic behaviour is best seen from the double logarithmic scale and indicates thermally controlled bubble growth. However, the time range until this regime sets in varies significantly with mixture ratio. Thermal effects set in earlier for heptane-rich mixtures, which is in line with the t_{c1} estimation above. It is interesting to note that the time delay to the onset of thermally controlled growth differs considerably between discrete fuel mixtures in figure 8(*a*) and pseudo-fuel mixtures in figure 8(*b*). The differences are even more pronounced in the linear representation of the initial growth phase, which is illustrated in close-ups A and B. Differences diminish for rising heptane percentage, so both fuel models converge to the pure heptane curve. On the other hand, differences between the fuel models are most pronounced for dodecane-rich mixtures.

The analysis of bubble growth rate is complemented by the liquid heat flux $q_w^L = \lambda_{m,w}^L (\partial T^L/\partial r)|_w$ and the bubble vapour content m_{vap}, whose time progressions are not discussed in detail here but are presented in § 6.1 of the supplementary material. In particular, q_L^w shows a pattern similar to that for $\dot{R}$. Distinctive differences between the discrete fuel and pseudo-fuel mixture models are also reflected in q_w^L and m_{vap}.

Summarizing, bubble growth dynamics diverges successively between discrete fuel and pseudo-fuel mixture for declining heptane percentage. The differences can be traced back to a local fuel segregation in the discrete fuel model, as shown in what follows, for example for a 05/95 % dodecane-rich mixture ratio.

4.2.4. *Binary heptane/dodecane mixtures at 303.15 K: local flow and temperature field*

As shown above, bubble growth dynamics diverges between the discrete fuel and pseudo-fuel models, most pronounced for dodecane-rich mixtures. In figure 8, the 05/95 % heptane/dodecane mixture has been marked by a dashed line. For example, for this mixture ratio, we substantiate the difference by a local flow and temperature field analysis in an early phase of bubble growth. Selected instants of time 0–9 have been marked in figure 8, in close-ups A and B. For these instants, radial profiles of the liquid fuel mass fraction $y_{Fuel}^L = y_{Hep}^L + y_{Dod}^L$ are depicted in figure 9(*a*). The bubble wall is located at $r - R = 0$. A distinctive boundary layer of y_{Fuel}^L develops whose thickness rises in the course of time. The boundary layer is slightly thicker for the discrete fuel mixture, albeit the differences

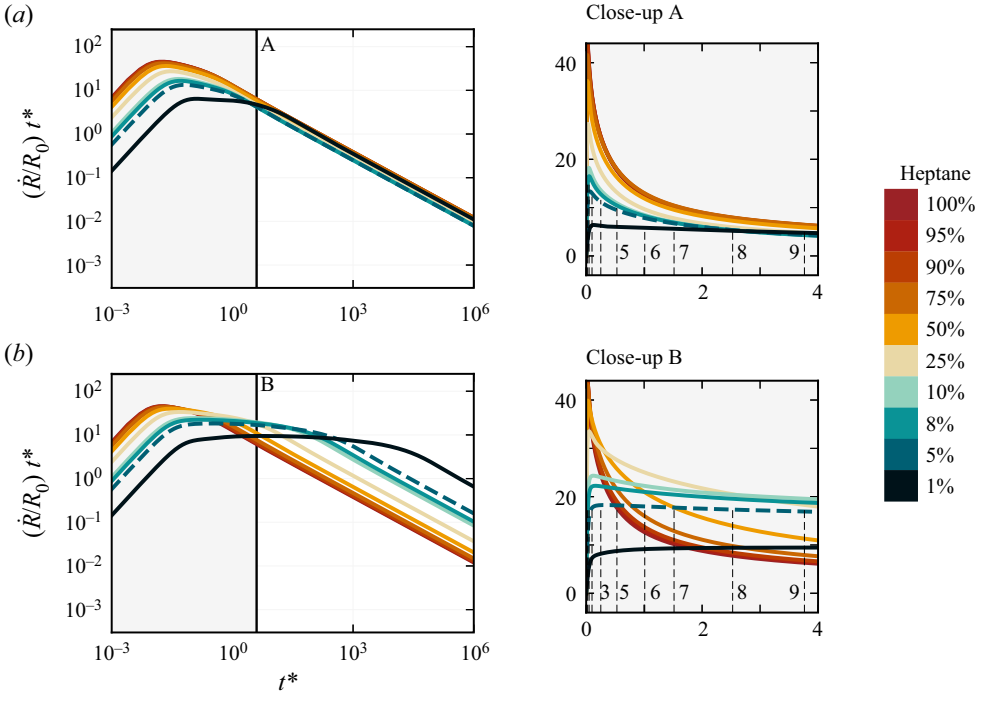

Figure 8. Time progression of bubble growth rate $\dot{R}$ for (a) discrete fuel and (b) pseudo-fuel mixtures, in the range 100/0 % to 01/99 % heptane/dodecane mixture ratio. Pure heptane corresponds to the 100/0 % heptane/dodecane mixture. The 05/95 % mixture ratio is marked by a dashed line.

to the pseudo-fuel mixture results are small. Thus regarding the liquid fuel mass fraction, pseudo-fuel mixture results deviate only slightly from their discrete fuel counterpart. The same holds for the fuel mass fraction within the bubble y^G_{Fuel}, which is reported in § 6.2 of the supplementary material.

Profiles of the liquid temperature T^L are illustrated in figure 9(b). For both discrete fuel and pseudo-fuel mixtures, $\partial T^L/\partial r|_w > 0$, which means that heat q^L_w is transferred from the liquid towards the bubble wall. However, T^L profiles of the pseudo-fuel mixture temporally precede the discrete fuel mixture profiles, so that the profiles of both fuel models diverge successively with time progress. The different liquid temperature distribution is reflected in significant deviations of the T^G distribution, which are also presented in § 6.2 of the supplementary material.

The different terms q^L_w, q^G_w and $L_m\dot{m}''_{Fuel}$ of the heat balance equation (2.20) are illustrated in figure 10 for the initial phase of bubble growth. In addition to the fuel mixture, pure heptane is included as a reference. For any fuel, q^L_w is larger than q^G_w by about three to four orders of magnitude. Thus q^L_w and $L_m\dot{m}''_{Fuel}$ have almost the same magnitude, and the residual heat flux q^G_w used for heating or cooling the bubble contents is small. This means that essentially the entire amount of q^L_w is used for vaporization of the liquid by the latent heat flux $L_m\dot{m}''_{Fuel}$.

The individual heat flux terms differ between the discrete fuel and pseudo-fuel models. In particular, the liquid wall heat flux q^L_w is considerably larger for the pseudo-fuel model than for the discrete fuel model. This observation coincides with a larger radial

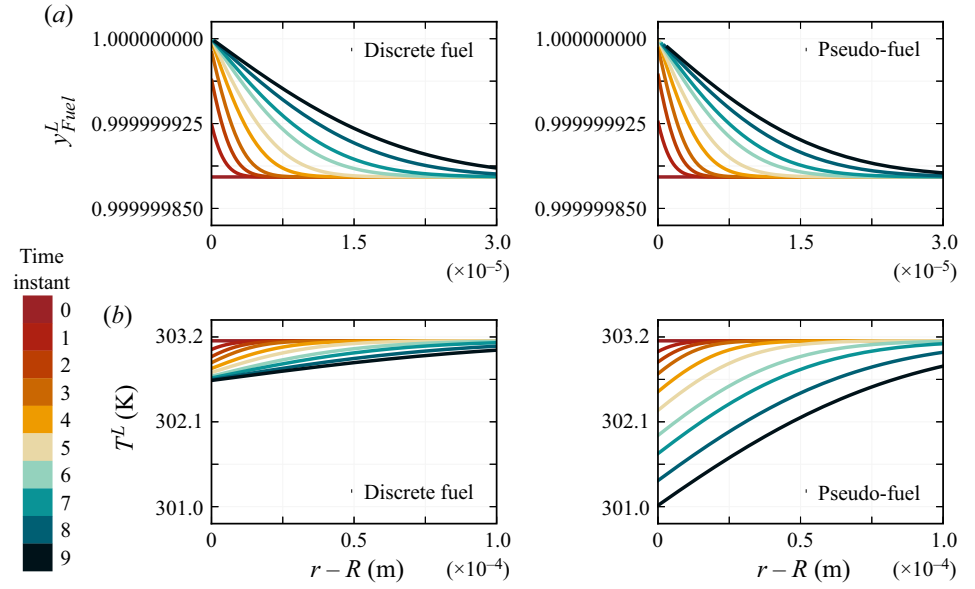

Figure 9. Radial distribution of (*a*) liquid mass fraction and (*b*) liquid temperature, for the 05/95 % heptane/dodecane mixture for both discrete fuel (left) and pseudo-fuel (right).

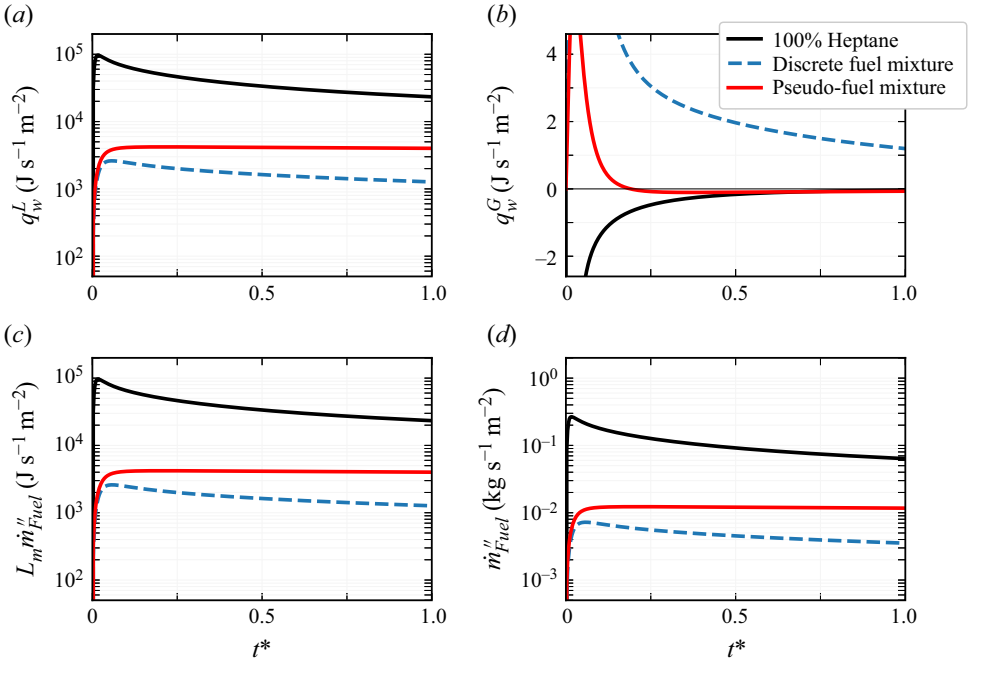

Figure 10. Time progression of heat flux on (*a*) the liquid side q^L_w and (*b*) the gaseous side q^G_w, and (*c*) the latent heat flux $L_m \dot{m}''_{Fuel}$ and (*d*) the mass flux $\dot{m}''_{Fuel}$ for the 05/95 % heptane/dodecane mixture. As a reference, pure heptane (100/0 % mixture) is included.

wall gradient of T_w^L by $q_w^L = \lambda_{m,w}^L(\partial T^L/\partial r)|_w$. Different liquid temperature profiles can be traced back to differences of latent heat flux $L_m\dot{m}''_{Fuel}$. Differences of $L_m\dot{m}''_{Fuel}$ in turn correlate with differences of the mass flux $\dot{m}''_{Fuel}$, as a cross-check between figures 10(*c*) and 10(*d*) shows. Thus albeit the mass flux is so small that its effect on the Rayleigh–Plesset equation (2.12) is insignificant, its effect on latent heat flux is not, due to the large magnitude of latent heat L_m. In other words, a kind of leverage effect is induced by L_m, so that albeit the magnitude of mass flux is small, even slight mass flux differences between the discrete fuel and pseudo-fuel models affect latent heat flux $L_m\dot{m}''_{Fuel}$ considerably. Therefore, we can conclude that the different characteristics of bubble growth dynamics that have been observed in figure 8 can be traced back to different latent heat flux characteristics of the discrete fuel and pseudo-fuel models.

Differences of $\dot{m}''_{Fuel}$ between the discrete fuel and pseudo-fuel models are associated directly with a local segregation of the liquid fuel in the discrete mixture, which is discussed next.

4.2.5. *Binary heptane/dodecane mixtures at 303.15 K: local fuel segregation*

For the discrete fuel model and for a 05/95 % heptane/dodecane mixture ratio, we discuss the radial profiles of the species mass fractions y^γ_{Hep}, y^γ_{Dod} and y^γ_{Air}, with $\gamma = G$ or L. For the gaseous bubble interior ($\gamma = G$), a rather homogeneous distribution of y^G_{Hep}, y^G_{Dod} and y^G_{Air} is present, thus vapour segregation is moderate. Results in the bubble interior are presented in § 6.3 of the supplementary material. The radial profiles of the species mass fractions in the liquid phase ($\gamma = L$) are depicted in figure 11. Distinctive boundary layers develop for any species. Wall mass fraction $y^L_{Hep,w}$ drops continuously and $y^L_{Dod,w}$ rises continuously in the course of time. Hence a segregation of liquid fuel occurs in the immediate wall proximity, and the mixture gets leaner and richer, with regard to heptane and dodecane, respectively. This means that the initial mixture ratio 05/95 % is shifted considerably towards a lower heptane percentage in the bubble wall proximity. This observation also holds for any other mixture ratio besides 05/95 % heptane/dodecane (not shown here). After summing y^L_{Hep} and y^L_{Dod}, the entire y^L_{Fuel} distribution is obtained, which has been shown in figure 9(*a*). Interestingly, y^L_{Fuel} differs only insignificantly between the discrete fuel and pseudo-fuel models, although a characteristic redistribution of y^L_{Hep} and y^L_{Dod} by local segregation occurs in the discrete model.

According to (2.2), the species mass flow rate $\dot{m}_\alpha$ is composed of the convective and diffusive mass flow rates, with $\dot{m}_{\alpha,conv} = -4\pi R^2\rho^L_{m,w}y^L_{\alpha,w}(u^L_w - \dot{R})$ and $\dot{m}_{\alpha,diff} = 4\pi R^2\rho^L_{m,w}D^L_{\alpha,w}(\partial y^L_\alpha/\partial r)|_w$. In figures 12(*a*,*b*), $\dot{m}_{Hep}$ and $\dot{m}_{Dod}$ are disaggregated in their contributions $\dot{m}_{Hep,conv}$ and $\dot{m}_{Hep,diff}$ as well as $\dot{m}_{Dod,conv}$ and $\dot{m}_{Dod,diff}$, respectively. As already illustrated in § 4.1.2 on the rapid pressure drop, $\dot{m}_{conv}$ and $\dot{m}_{diff}$ are oriented in the same direction for the high-volatile heptane, and flow in opposite directions for the low-volatile dodecane. Due to the small heptane mass fraction $y^L_{Hep,w}$, the convective part $\dot{m}_{Hep,conv}$ of heptane mass flow rate is minor (note the augmentation by factor 10 illustration of $\dot{m}_{Hep,conv}$ in figure 12*a*), and $\dot{m}_{Hep}$ is governed by the diffusive part $\dot{m}_{Hep,diff}$. Additionally, $y^L_{Hep,w}$ is reduced by local fuel segregation, so convection is lessened even further. For dodecane, according to figure 12(*b*), the convective and diffusive mass flow rates essentially cancel out, so that in summary, $\dot{m}_{Dod}$ is very small. Summing all species mass flow rate contributions $\dot{m}_{Hep,conv}$, $\dot{m}_{Hep,diff}$, $\dot{m}_{Dod,conv}$ and $\dot{m}_{Dod,diff}$, we

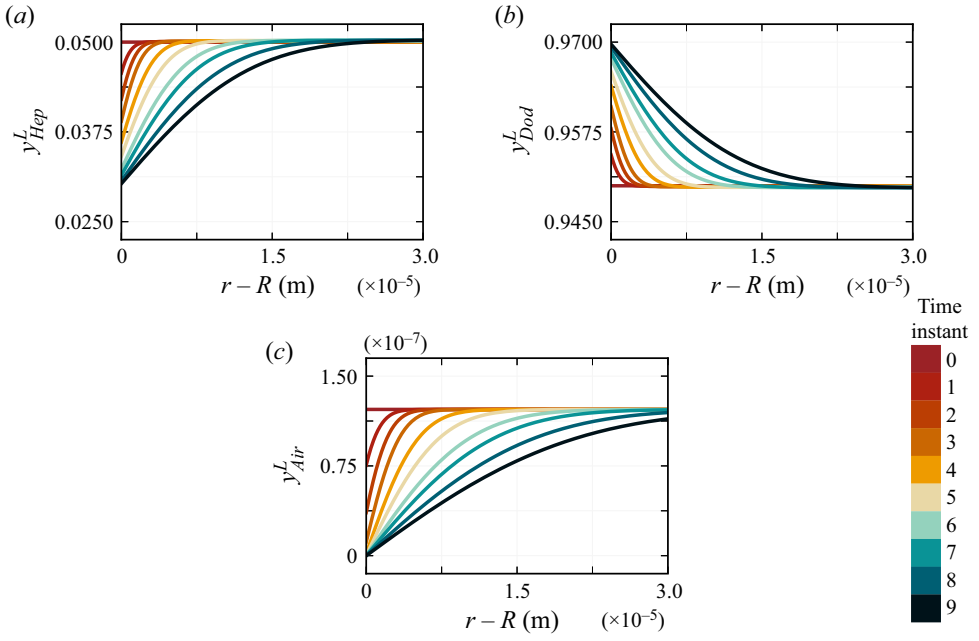

Figure 11. Radial distribution of mass fraction in the liquid around the bubble for the discrete 05/95 % heptane/dodecane mixture. (*a*) Heptane, (*b*) dodecane and (*c*) air mass fraction within liquid.

obtain the entire fuel mass flow rate $\dot{m}_{Fuel}$. In order to clarify that it is the fuel mass flow rate of the discrete fuel model, we term it $\dot{m}_{Fuel,discr}$ in figure 12(*c*). As discussed above, $\dot{m}_{Fuel,discr}$ is governed completely by the diffusive heptane mass flow rate $\dot{m}_{Hep,diff}$.

In figure 12(*c*), the corresponding result obtained by the pseudo-fuel model, $\dot{m}_{Fuel,pseudo}$, is also shown. Here, $\dot{m}_{Fuel,pseudo}$ rises disproportionately fast and is already one order of magnitude larger than $\dot{m}_{Fuel,discr}$ at the end of the early time range considered in figure 12 – note the demagnified illustration of $\dot{m}_{Fuel,pseudo}$ in figure 12(*c*).

In figure 12(*d*), $\dot{m}_{Fuel,pseudo}$ is split into its convective and diffusive parts. Since for the pseudo-fuel, fuel species interdiffusion is by definition absent, mass flow is dominated by the convective part. It should be pointed out that a small diffusion between pseudo-fuel and air is of course present, but it is minor for the test case under consideration. Thus convection governs mass flow in the pseudo-fuel model, while it is diffusion that does so in the discrete model. In summary, the entire mass flow rate $\dot{m}_{Fuel,pseudo}$ of the pseudo-fuel is one order of magnitude larger than $\dot{m}_{Fuel,discr}$ of the discrete fuel.

Now we have discovered the origin of the differences between discrete fuel and pseudo-fuel model. Obviously, interdiffusion of fuel species and the corresponding fuel segregation dominate the mass transfer for the discrete fuel: the diffusive and convective mass flow rates of dodecane essentially cancel out. On the other hand, the convective mass flow rate of heptane is much smaller than the diffusive mass flow rate, due to the small heptane concentration. In summary, a rather small net mass flow rate of heptane, which is governed by diffusion, enters the bubble interior. Fuel species interdiffusion is by definition absent in the pseudo-fuel. Here, convection governs the mass transfer of the single-component pseudo-fuel. Thus we can conclude that the simplification introduced in the pseudo-fuel – i.e. the absence of fuel species interdiffusion – falsifies the mass flow rate. For example, in the 05/95 % heptane/dodecane mixture, the mass flow rate is

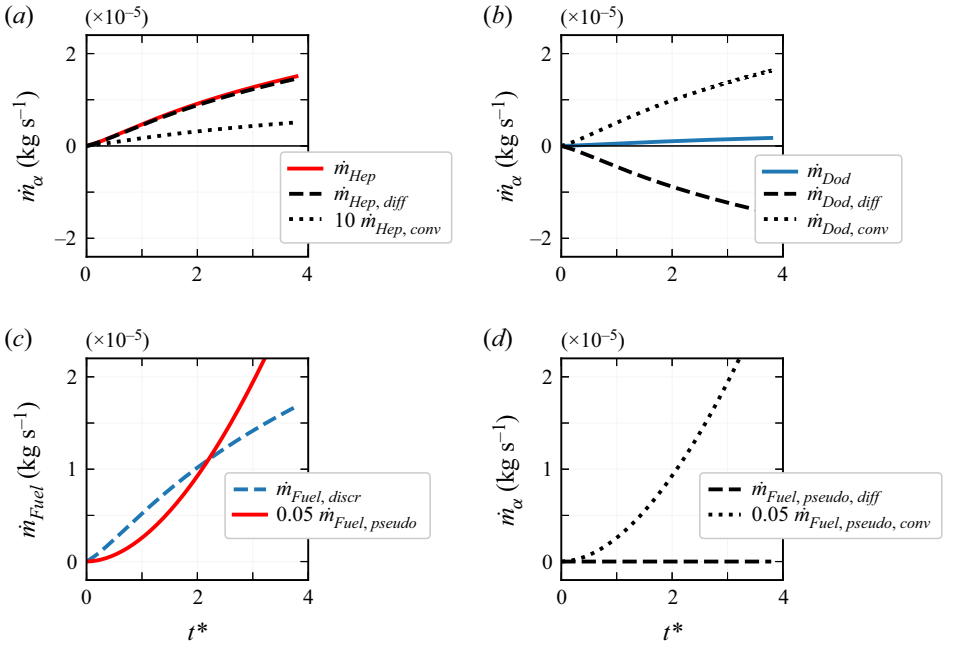

Figure 12. Convective and diffusive contributions to the (*a*) heptane and (*b*) dodecane mass flows of a discrete 05/95 % heptane/dodecane mixture. Panel (*c*) shows the entire mass flow of the discrete fuel and the corresponding pseudo-fuel mixture, and (*d*) shows the convective and diffusive parts of the pseudo-fuel mixture.

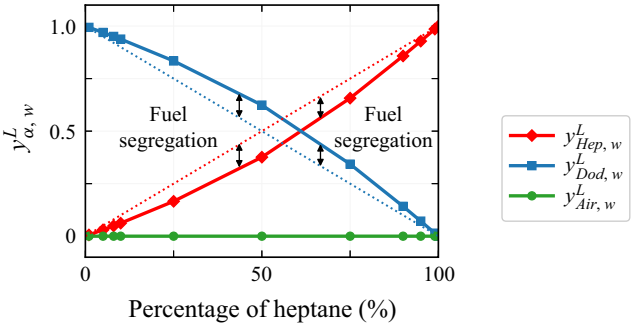

Figure 13. Mass fraction of heptane, dodecane and air at the liquid side of the bubble wall for $t^* = 10^6$ and a discrete fuel mixture variation.

overestimated by one order of magnitude. This overestimation leads to an enhanced heat transfer by latent heat flux, and to the considerable differences in bubble growth dynamics observed between discrete fuel and pseudo-fuel, as discussed above.

A similar segregation process was observed for the rapid pressure drop in § 4.1 during the bubble expansion phase. For an oscillating bubble, however, expansion and compression have alternated regularly, until bubble oscillation has abated. Hence the direction of the segregation changed regularly, and the residual segregation was moderate, according to figure 3. On the other hand, for continuous bubble growth in superheated liquid, a persistent segregation with wall-adjacent heptane depletion and dodecane

enrichment occurs, which shifts the near-wall liquid mixture ratio towards a leaner heptane percentage and a richer dodecane percentage than the initial one.

This result is summarized by an illustration of the species mass fractions at both sides of the bubble wall. In § 6.4 of the supplementary material, more details are presented, while here, we confine ourselves to the liquid side of the bubble wall. In figure 13, $y^L_{Hep,w}$, $y^L_{Dod,w}$ and $y^L_{Air,w}$ are shown for several initial mixture ratios at $t^* = 10^6$, which is the end of the time range considered. The initial mixture ratio is illustrated by straight dotted lines. Fuel segregation is well discernible by the deviation of the species wall mass fraction from the initial mixture ratio, and is most significant for the 50/50 % mixture.

5. Conclusions and outlook

A mathematical model has been presented that enables the simulation of segregation of binary alkane mixtures and air due to spherical bubble dynamics. Detailed heat and mass transfer and phase transition are resolved. For example, high-volatile heptane and low-volatile dodecane are considered. Subject to the volatility of the components, the convective and diffusive mass fluxes over the bubble interface are oriented in the same and opposite directions for the higher- and lower-volatile components, respectively. This fuel species interdiffusion and the staggered mass flow of components leads to a local mixture segregation in the liquid surrounding the bubble. A comparative study with a pseudo-fuel whose components cannot segregate reveals that for an oscillating bubble, the local segregation hardly affects bubble dynamics, while for a continuously growing bubble, the growth rate and thus other temporal characteristics are considerably affected, particularly for a low heptane percentage. The simplification introduced in the pseudo-fuel falsifies the mass flow rate. For the conditions considered, the mass flow rate is overestimated by one order of magnitude. Different mass flow rates mainly affect heat transfer due to differences in latent heat flux.

This study demonstrates limitations of a surrogate mixture where both components are treated like a pseudo-fluid. Such surrogates are the basis for e.g. mass transfer cavitation models in recent CFD methods. Bubble growth is often associated with cavitation in terms of evaporation and void creation in this model family. In particular for continuous bubble growth, these first results on bubble dynamics in segregation-prone binary alkane mixtures create doubt about the extent of validity of mass transfer cavitation models for real fluids as e.g. fuels or hydraulic oils. Further studies with a variation of e.g. further mixture components and a broader parameter range are suggested to assess the impact of local mixture segregation on bubble dynamics.

We assume that this study may be the basis for the development of multi-component mass transfer cavitation models, and at the same time, for improved CFD methods for real fluid-mixture applications. In a next step, we plan a direct embedding of a multiplicity of single Lagrange bubbles into the Eulerian framework of a 3-D CFD method. By the homobaricity assumption, the computational effort of each single bubble is reduced considerably and thereby opens the opportunity to embed a large number of single bubbles into a 3-D Euler–Lagrange framework in future studies.

For a more thorough assessment of the mathematical model, a validation by experimental data is indispensable. This study may also serve as a starting point for setting up purposeful experiments on single-bubble dynamics in fluid mixtures.

Supplementary material. Supplementary material is available at https://doi.org/10.1017/jfm.2022.636.

Funding. This work was supported by the German Research Foundation (DFG), grant no. 355240670.

Declaration of interests. The authors report no conflict of interest.

Author ORCIDs.
J.M. Bermudez-Graterol https://orcid.org/0000-0002-7604-2173;
R. Skoda https://orcid.org/0000-0003-3289-083X.

Appendix A. Details of the mathematical model

A.1. *Model assumptions*

The assumptions made can be summarized as follows.

- The bubble is spherically symmetric, i.e. bubble wall motion and transport processes are considered in the radial direction only.
- Bubble wall motion and the interface location are evaluated by the Rayleigh–Plesset equation.
- Thermal and phase equilibrium is assumed at the bubble wall. This assumption has been justified by a comparative assessment of equilibrium versus non-equilibrium bubble wall boundary conditions (Bermudez-Graterol *et al.* 2021). For a water–air system, Bermudez-Graterol *et al.* (2021) have shown that non-equilibrium affects only insignificantly the heat and mass transfer even during the latest stages of bubble collapse. Moreover, there is no generalized non-equilibrium approach available for fluid mixtures to the best of our knowledge, so we maintain the equilibrium condition in this study.
- The bubble centre is stationary.
- Assuming phase equilibrium, Raoult's law is employed to formulate bubble interface conditions on the concentration.
- Vaporous alkane components and air within the bubble are an ideal mixture of thermally and calorically ideal gases.
- We assume that dissolved air is diluted in the liquid fuel, thus air at the bubble wall obeys Henry's law.
- Homobaricity holds within the bubble, i.e. pressure is homogeneous in the radial direction.
- In the liquid, we note that the flow is irrotational and thus potential, so that pressure obeys Bernoulli's equation.
- Fick's law holds for mass diffusion due to concentration gradients. Since the temperature and pressure levels in this study are moderate, the effects of pressure diffusion due to pressure gradients and thermal diffusion due to temperature gradients are neglected.

It should be noted that the assumption of an ideal gas holds only if the pressure is well below the critical pressure. Also, Henry's law holds only for low pressure. Due to the moderate pressure level in this study, we assume that assuming an ideal gas and Henry's law are valid.

A.2. *Governing equations within the bubble*

It is assumed that the specific heat and gas constants of vapour components as well as air are constant. Mixture values are evaluated by a weighted mean:

$$\Phi_m^G = y_{Hep}^G \Phi_{Hep}^G + y_{Dod}^G \Phi_{Dod}^G + y_{Air}^G \Phi_{Air}^G. \tag{A1}$$

In (A1), Φ may correspond to internal energy e, enthalpy h, or specific heat c_p or c_v, with $h = e + p/\rho$. The specific gas constant is obtained by $\mathcal{R}_\alpha = \mathcal{R}_{Univ}/M_\alpha$, with $\mathcal{R}_{Univ} = 8314\,\mathrm{J\,kmol^{-1}\,K^{-1}}$ and M_α as the molar mass of species α. Partial pressure is evaluated for a thermally ideal gas by $p^G_\alpha = \rho^G_\alpha \mathcal{R}_\alpha T^G$, where T is the temperature. Mixture pressure fulfils Dalton's law, $p^G = p^G_{Hep} + p^G_{Dod} + p^G_{Air}$, so the ideal gas law also holds for p^G:

$$p^G = \rho^G_m \mathcal{R}_m T^G. \tag{2.4}$$

It should be pointed out that although p^G is spatially homogeneous within the bubble, its contributions p^G_{Hep}, p^G_{Dod} and p^G_{Air} usually are not. Since the gaseous species are also calorically ideal, $e^G_\alpha = c^G_{v,\alpha} T^G$ and $h^G_\alpha = c^G_{p,\alpha} T^G$, and also for the mixture properties, $e^G_m = c^G_{v,m} T^G$ and $h^G_m = c^G_{p,m} T^G$ hold.

The mixture energy conservation, neglecting viscous effects, reads

$$\frac{\partial(\rho^G_m e^G_m)}{\partial t} + \frac{1}{r^2}\frac{\partial}{\partial r}(r^2 \rho^G_m h^G_m u^G) = -\frac{1}{r^2}\frac{\partial}{\partial r}(r^2 q^G). \tag{A2}$$

The heat flux q^G is evaluated by

$$q^G = -\lambda^G_m \frac{\partial T^G}{\partial r} - \rho^G_m \sum_{\alpha=1}^{N_S} D^G_\alpha h^G_\alpha \frac{\partial y^G_\alpha}{\partial r}, \tag{A3}$$

where λ is the thermal conductivity. In the second term on the right-hand side of (A3), α is summed over all $N_S = 3$ species, which means $\alpha = Hep$, Dod and Air. The first part of the right-hand side of (A3) corresponds to Fourier's law and means the heat transport by conduction, and the second part describes the heat transport by each of the diffusing components. Employing the homobaricity assumption $\partial p^G/\partial r = 0$, expressions for the velocity profile and the pressure are obtained according to (2.5)–(2.7).

A.3. *Boundary conditions at the bubble wall*

Assuming phase equilibrium, Raoult's law in terms of (2.19) with $\gamma_\alpha = 1$ is employed to formulate interface conditions on the concentration:

$$\gamma_\alpha x^L_{\alpha,w} p^{Sat}_\alpha|_{T^L_w} = x^G_{\alpha,w} p^G. \tag{2.19}$$

In figure 14, experimentally measured vapour–liquid equilibria by Maia de Oliveira *et al.* (2002) are presented for temperature and pressure ranges which are relevant for this study. The evaluation of (2.19) shows a very good agreement to data, indicating that the assumption $\gamma_\alpha = 1$ is an acceptable approximation of the bubble interface condition for the heptane/dodecane mixture.

Using the mass fractions $y^L_{\alpha,w}$ and $y^G_{\alpha,w}$ rather than mole fractions $x^L_{\alpha,w}$ and $x^G_{\alpha,w}$,

$$x^L_{\alpha,w} = y^L_{\alpha,w} \frac{M^L_{m,w}}{M_\alpha}, \tag{A4}$$

$$x^G_{\alpha,w} = y^G_{\alpha,w} \frac{M^G_{m,w}}{M_\alpha}, \tag{A5}$$

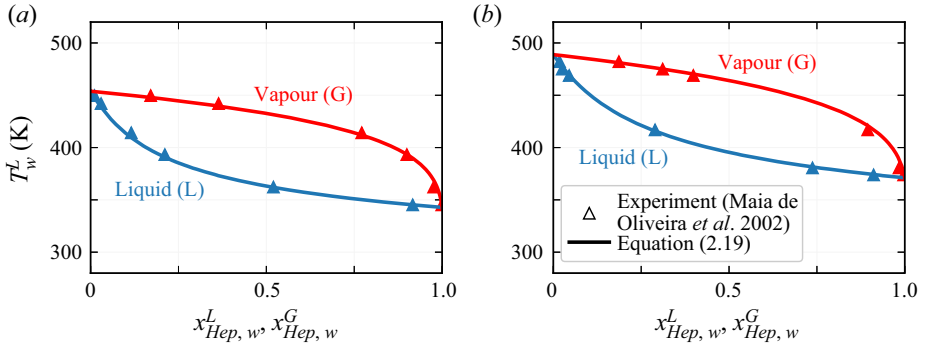

Figure 14. Vapour–liquid equilibrium for a heptane/dodecane mixture for (*a*) $p^G = 0.4$ bar and (*b*) $p^G = 1.0$ bar.

we obtain the phase equilibrium relation

$$y^L_{\alpha,w}\frac{M^L_{m,w}}{M_\alpha}p^{Sat}_\alpha|_{T^L_w} = y^G_{\alpha,w}\frac{M^G_{m,w}}{M_\alpha}p^G, \tag{A6}$$

where $M^G_{m,w}$ and $M^L_{m,w}$ are the mixture molar mass at the gas and liquid sides of the bubble wall, respectively, including all species, i.e. $1/M^G_{m,w} = \sum_{\alpha=1}^{N_S} y^G_{\alpha,w}/M_\alpha$ and $1/M^L_{m,w} = \sum_{\alpha=1}^{N_S} y^L_{\alpha,w}/M_\alpha$, where α is summed over all $N_S = 3$ species. It is preferred that (A6) is implemented in the computer code rather than (2.19).

Henry's law is given by

$$p^G_{Air,w} = x^L_{Air,w}H_m. \tag{2.23}$$

The Henry coefficient H_m depends on T^G_w and the liquid mixture state, as will be explicated in § A.4.3. By utilizing the mass fraction rather than the mole fraction, and noting $p^G_{Air,w} = x^L_{Air,w}p^G$, we obtain

$$y^L_{Air,w} = \frac{M_{Air}}{M^L_{m,w}H_m}y^G_{Air,w}\frac{\mathcal{R}_{Air}}{\mathcal{R}_{m,w}}p^G, \tag{A7}$$

where $M^L_{m,w}$ is the mixture molar mass at the liquid side of the bubble wall, $1/M^L_{m,w} = \sum_{\alpha=1}^{N_S} y^L_{\alpha,w}/M_\alpha$. Equation (A7) is used to implement Henry's law, rather than (2.23).

A.4. *Thermophysical properties*

A.4.1. *Liquid phase*

Due to the small amount of air dissolved in the liquid, we assume that property changes due to dissolved air can be neglected, so that liquid mixture properties ρ^L_m, c^L_m, μ^L_m and λ^L_m are evaluated merely with the alkane mixture components, which means $N_F = 2$ mixture components. The mixture rules are only summarized here, and details can be found in the specific citations. Although most of the rules are compiled in classical textbooks, e.g. Poling, O'Connell & Prausnitz (2001), we specify the original citation for completeness.

Liquid density ρ_m^L reads

$$\rho_m^L = \left(\sum_{\alpha=1}^{N_F} \frac{y_\alpha^L}{\rho_\alpha^L} \right)^{-1}. \tag{A8}$$

The density of pure alkane ρ_α^L is evaluated in dependence on T^L by Rackett (1970), modified by Spencer & Danner (1972). The specific heat c_m^L is evaluated by

$$c_m^L = \sum_{\alpha=1}^{N_F} y_\alpha^L c_\alpha^L. \tag{A9}$$

The alkane heat capacity c_α^L is evaluated in dependence on T^L by the approach of Bondi (1966). Liquid viscosity μ_m^L in (2.17) follows from the mixture rule by Grunberg & Nissan (1949):

$$\ln \mu_m^L = \sum_{\alpha=1}^{N_F} x_\alpha^L \ln \mu_\alpha^L + \frac{1}{2} \sum_{\alpha=1}^{N_F} \sum_{\beta=1}^{N_F} x_\alpha^L x_\beta^L \mathcal{G}_{\alpha,\beta}. \tag{A10}$$

The dynamic viscosity of heptane and dodecane are evaluated in dependence on T^L by the regression of van Velzen, Lopes Cardozo & Langenkamp (1972), and the binary interaction parameter $\mathcal{G}_{\alpha,\beta}$ is approximated according to Isdale, MacGillivray & Cartwright (1985). The thermal conductivity λ_m^L is approximated by Li's mixing rule (Li 1976):

$$\lambda_m^L = \sum_{\alpha=1}^{N_F} \sum_{\beta=1}^{N_F} \Psi_\alpha \Psi_\beta \lambda_{\alpha,\beta}. \tag{A11}$$

Here, $\lambda_{\alpha,\beta}$ is the harmonic mean of the individual thermal conductivities:

$$\lambda_{\alpha,\beta} = 2 \left(\frac{1}{\lambda_\alpha^L} + \frac{1}{\lambda_\beta^L} \right)^{-1}. \tag{A12}$$

The dimensionless parameter Ψ_α is determined by the mole fractions x_α^L and molar volumes v_α^L:

$$\Psi_\alpha = \frac{x_\alpha^L v_\alpha^L}{\sum_{\beta=1}^{N_F} x_\beta^L v_\beta^L}, \tag{A13}$$

with $v_\alpha^L = M_\alpha / \rho_\alpha^L$, which has unit $\mathrm{m}^3\ \mathrm{kmol}^{-1}$. Thermal conductivity of heptane and dodecane are evaluated according to Latini & Pacetti (1977), again in dependence on T^L. For the algorithm, we refer to the original paper.

So far, for the evaluation of ρ_m^L, c_m^L, μ_m^L and λ_m^L, dissolved air has not been considered due to its small effect. In contrast, air diffusion in the alkane mixture is important. The air diffusion coefficient D_{Air}^L is evaluated by the mixing rule of Perkins & Geankoplis (1969):

$$D_{Air}^L = \frac{1}{(\mu_m^L)^{0.8}} \sum_{\beta=1}^{N_F} x_\beta^L D_{Air,\beta,o}^L (\mu_\beta^L)^{0.8}. \tag{A14}$$

Due to the low concentration of dissolved air, $D_{Air,\beta,o}^L$ is estimated by the assumption of infinite dilution of air in the liquid mixture, according to the Wilke–Chang approximation

(Wilke & Chang 1955)

$$D^L_{Air,\beta,o} = \frac{7.4 \times 10^{-15} \sqrt{\phi_\beta M_\beta}\, T^L}{\mu^L_\beta (v^L_{b,Air} \times 10^3)^{0.6}}, \tag{A15}$$

with the dimensionless association factor ϕ_β of the solvent $\beta = Hep$ or Dod, which is assumed to equal $\phi_\beta = 1$ for any alkane, and the molar volume of the solute, i.e. air at its normal boiling point (at atmospheric pressure), is $v^L_{b,Air} = 0.03$ m^3 kmol^{-1}.

The diffusion coefficients of the alkanes D^L_α are evaluated in two steps. First, an infinite dilution is assumed, and the empirical equation of Hayduk & Minhas (1982) is employed:

$$D^L_{\alpha,\beta,o} = 13.3 \times 10^{-12} \frac{(T^L)^{1.47} (10^3 \mu^L_\beta)^\varepsilon}{(10^3 v^L_{b,\alpha})^{0.71}}, \tag{A16}$$

with $\varepsilon = 10.2/(10^3 v^L_{b,\alpha}) - 0.791$, which is dimensionless. Here, α corresponds to either Hep or Dod, and β to the respective other alkane species; $v^L_{b,\alpha}$ is again the molar volume at its normal boiling point and is given by $v^L_{b,\alpha} = M_\alpha/\rho^L_\alpha|_{T_{b,\alpha}}$ with $T_{b,Hep} = 327$ K and $T_{b,Dod} = 490$ K. In a second step, from the diffusion coefficient for infinite dilution $D^L_{\alpha,\beta,o}$, the coefficient at any concentration is derived by the approximation of Vignes (1966):

$$D^L_\alpha = (D^L_{\alpha,\beta,o})^{1-x^L_\alpha} (D^L_{\beta,\alpha,o})^{x^L_\alpha}. \tag{A17}$$

A.4.2. *Gaseous phase*

In the bubble, a mixture of fuel vapour and air is present. As already noted in § A.2, mixture internal energy e^G_m and enthalpy h^G_m as well as specific isobaric and isochoric heat capacities $c^G_{p,m}$ and $c^G_{v,m}$, are linearly weighted by mass fraction and the corresponding vapour and air values of $c^G_{p,\alpha}$. For vapour ($\alpha = Hep$ or Dod), $c^G_{p,\alpha}$ is obtained in dependence on T^G by regressions provided by Daubert & Danner (1989). We obtain $c^G_{p,Air}$ by

$$c^G_{p,Air} = \frac{\kappa_{Air}\, \mathcal{R}_{Air}}{\kappa_{Air} - 1}, \tag{A18}$$

with $\mathcal{R}_{Air} = \mathcal{R}_{Univ}/M_{Air}$. The dimensionless isentropic exponent κ_α is evaluated by the NIST database (Linstrom & Mallard 2016) at $T^G = 400$ K and $p^G = 1.013$ bar. We obtain $c^G_{v,\alpha}$ for any species α by

$$c^G_{v,\alpha} = c^G_{p,\alpha} - \mathcal{R}_\alpha = \frac{\mathcal{R}_\alpha}{\kappa_\alpha - 1}. \tag{A19}$$

The mixture gas constant $\mathcal{R}_m$ is also evaluated by a linear weighted mean of specific gas constants $\mathcal{R}_\alpha = \mathcal{R}_{Univ}/M_\alpha$, with $M_{Hep} = 100.2$ kg kmol^{-1}, $M_{Dod} = 170.3$ kg kmol^{-1} and $M_{Air} = 28.97$ kg kmol^{-1}:

$$\mathcal{R}_m = \sum_{\alpha=1}^{N_S} y^G_\alpha \mathcal{R}_\alpha. \tag{A20}$$

The thermal conductivity is assumed to be temperature-dependent and evaluated for the heptane/dodecane vapour mixture (vap) on the one hand and air on the other hand, and

afterwards the mixture rule by Brokaw (1955) is employed for approximating the mixture thermal conductivity λ_m^G:

$$\lambda_m^G = \frac{1}{2}\left[(x_{Hep}^G + x_{Dod}^G)\lambda_{vap}^G + x_{Air}^G\lambda_{Air}^G + \frac{1}{\dfrac{x_{Hep}^G + x_{Dod}^G}{\lambda_{vap}^G} + \dfrac{x_{Air}^G}{\lambda_{Air}^G}}\right]. \tag{A21}$$

The thermal conductivities of the vapour mixture, λ_{vap}^G, and air, λ_{Air}^G, are obtained by the corresponding states method of Chung, Lee & Starling (1984), and by the regression of Daubert & Danner (1989), respectively. Details on the formulations can be found in the original citations and are omitted here due to their length.

The diffusion coefficient for any species α is evaluated according to Bird *et al.* (1960):

$$D_\alpha^G = (1 - x_\alpha^G)\sum_{\substack{\beta=1 \\ \beta \neq \alpha}}^{N_S} \frac{x_\beta^G}{D_{\alpha,\beta}^G}. \tag{A22}$$

The diffusion coefficients between separate species $D_{\alpha,\beta}^G$ are approximated according to Fuller, Ensley & Giddings (1969) and read, rectified by SI units, as

$$D_{\alpha,\beta}^G = \frac{1.01116 \times 10^{-2}(T^G)^{1.75}(1/M_\alpha + 1/M_\beta)^{1/2}}{p^G[(\sum V_\alpha)^{1/3} + (\sum V_\beta)^{1/3}]^2}. \tag{A23}$$

The dimensionless atomic diffusion volumes $\sum V_\alpha$ are obtained by the molecule structures according to VDI e.V. (1994) and are $\sum V_{Hep} = 147.2$, $\sum V_{Dod} = 249.5$ and $\sum V_{Air} = 20.1$.

A.4.3. *Bubble wall*

Surface tension σ_α of alkanes is obtained by data from Daubert & Danner (1989), and σ_m is evaluated by a mole-fraction weight:

$$\sigma_m = \sum_{\alpha=1}^{N_F} x_\alpha^L \sigma_\alpha. \tag{A24}$$

Latent heat L_m is evaluated by the mixing rule presented by Tamim & Hallett (1995):

$$L_m = \sum_{\alpha=1}^{N_F} \epsilon \frac{L_\alpha}{M_\alpha}, \tag{A25}$$

with $\epsilon = \dot{m}_\alpha'' / \sum_{\alpha=1}^{N_F} \dot{m}_\alpha''$, which is dimensionless. The molar latent heat of alkane species L_α is obtained by an approximation according to Watson (1943):

$$L_\alpha = L_{b,\alpha}\frac{T_{c,\alpha} - T_w^L}{T_{c,\alpha} - T_{b,\alpha}}, \tag{A26}$$

where $T_{c,\alpha}$ is the critical temperature and corresponds to 540 and 658 K for heptane and dodecane, respectively, and $T_{b,\alpha}$ is the temperature at normal boiling point and

β	$H_{O_2,\beta}$	$H_{N_2,\beta}$
Heptane	4.964×10^7	7.406×10^7
Dodecane	4.404×10^7	7.741×10^7

Table 2. Henry coefficients $H_{\alpha,\beta}$ of O_2 and N_2 in alkanes (Hesse *et al.* 1996).

has already been given in § A.4.1. Latent heat at the normal boiling point $L_{b,\alpha}$ equals 317×10^6 J kmol^{-1} and 257×10^6 J kmol^{-1} for heptane and dodecane, respectively.

As for the surface tension, the mixture saturation pressure p_m^{Sat} is evaluated by a mole-fraction weight from the single alkane saturation pressures p_α^{Sat}, which are obtained by regressions from Daubert & Danner (1989):

$$p_m^{Sat} = \sum_{\alpha=1}^{N_F} x_\alpha^L p_\alpha^{Sat}. \tag{A27}$$

For the evaluation of the mixture Henry coefficient H_m, first the Henry coefficients for oxygen and nitrogen are estimated by the mixture rule of Gmehling *et al.* (2012):

$$\ln H_\alpha = \frac{\sum_{\beta=1}^{N_F} \frac{y_{\beta,w}^L}{M_\beta} H_{\alpha,\beta}}{\sum_{\beta=1}^{N_F} \frac{y_{\beta,w}^L}{M_\beta}}, \tag{A28}$$

where α equals either oxygen O_2 or nitrogen N_2. For Henry coefficients $H_{\alpha,\beta}$ of O_2 and N_2 in alkanes, no temperature dependence could be found in the literature, hence they are assumed constant and are summarized in table 2.

Once H_{O_2} and H_{N_2} have been obtained by (A28), H_m is evaluated by a simple mass-fraction weight of oxygen and nitrogen:

$$H_m = 0.24 H_{O_2} + 0.76 H_{N_2}. \tag{A29}$$

References

Ali, A. & Ake, S.B. 2016 A new formulation and analysis of a collapsing bubble with different content in a liquid induced during acoustic cavitation. *Intl J. Numer. Meth. Heat Fluid Flow* **26** (6), 1729–1746.

Arefmanesh, A., Advani, S.G. & Michaelides, E.E. 1992 An accurate numerical solution for mass diffusion-induced bubble growth in viscous liquids containing limited dissolved gas. *Intl J. Heat Mass Transfer* **35** (7), 1711–1722.

Bader, A., Keller, P. & Hasse, C. 2013 The influence of non-ideal vapor–liquid equilibrium on the evaporation of ethanol/iso-octane droplets. *Intl J. Heat Mass Transfer* **64**, 547–558.

Bergamasco, L. & Fuster, D. 2017 Oscillation regimes of gas/vapor bubbles. *Intl J. Heat Mass Transfer* **112**, 72–80.

Bermudez-Graterol, J.M., Nickaeen, M. & Skoda, R. 2021 Numerical simulation of spherical bubble collapse by a uniform bubble pressure approximation and detailed description of heat and mass transfer with phase transition. *Appl. Math. Model.* **96**, 80–110.

Bird, R.B., Stewart, W.E. & Lightfoot, E.N. 1960 *Transport Phenomena*. Wiley.

Board, S.J. & Duffey, R.B. 1971 Spherical vapour bubble growth in superheated liquids. *Chem. Engng Sci.* **26** (3), 263–274.

Bondi, A. 1966 Estimation of heat capacity of liquids. *Ind. Engng Chem. Fundam.* **5** (4), 442–449.

BRENNEN, C.E. 1995 *Cavitation and Bubble Dynamics*. Oxford University Press.

BROKAW, R.S. 1955 Estimating thermal conductivities for nonpolar gas mixtures. *Ind. Engng Chem.* **47** (11), 2398–2400.

CHERNOV, A.A., PIL'NIK, A.A., VLADYKO, I.V. & LEZHNIN, S.I. 2020 New semi-analytical solution of the problem of vapor bubble growth in superheated liquid. *Sci. Rep.* **10** (1), 16526.

CHUNG, T.H., LEE, L.L. & STARLING, K.E. 1984 Applications of kinetic gas theories and multiparameter correlation for prediction of dilute gas viscosity and thermal conductivity. *Ind. Engng Chem. Fundam.* **23** (1), 8–13.

CRANK, J. & NICOLSON, P. 1996 A practical method for numerical evaluation of solutions of partial differential equations of the heat-conduction type. *Adv. Comput. Math.* **6** (1), 207–226.

CRUM, L.A. 1984 Acoustic cavitation series: part five rectified diffusion. *Ultrasonics* **22** (5), 215–223.

DAUBERT, T.E. & DANNER, R.P. 1989 *Physical and Thermodynamic Properties of Pure Chemicals Data Compilation*. Hemisphere Publishing Corporation.

DELALE, C.F & PASINLIOĞLU, Ş. 2015 First iterative solution of the thermal behaviour of acoustic cavitation bubbles in the uniform pressure approximation. *J. Phys.: Conf. Ser.* **656**, 012016.

DERGARABEDIAN, P. 1953 The rate of growth of vapor bubbles in superheated water. *Trans. ASME J. Appl. Mech.* **20** (4), 537–545.

DOROFEEVA, I.E., THOMAS, F.O. & DUNN, P.F. 2009 Cavitation of JP-8 fuel in a converging–diverging nozzle: experiments and modelling. In *Proceedings of the 7th International Symposium on Cavitation*. University of Michigan.

DUNN, P.F., THOMAS, F.O., DAVIS, M.P. & DOROFEEVA, I.E. 2010 Experimental characterization of aviation-fuel cavitation. *Phys. Fluids* **22** (11), 117102.

FORSTER, H.K. & ZUBER, N. 1954 Growth of a vapor bubble in a superheated liquid. *J. Appl. Phys.* **25** (4), 474–478.

FUJIKAWA, S. & AKAMATSU, T. 1980 Effects of the non-equilibrium condensation of vapour on the pressure wave produced by the collapse of a bubble in a liquid. *J. Fluid Mech.* **97** (3), 481–512.

FULLER, E.N., ENSLEY, K. & GIDDINGS, J.C. 1969 Diffusion of halogenated hydrocarbons in helium. The effect of structure on collision cross sections. *J. Phys. Chem.* **73** (11), 3679–3685.

FUSTER, D. & MONTEL, F. 2015 Mass transfer effects on linear wave propagation in diluted bubbly liquids. *J. Fluid Mech.* **779**, 598–621.

GARTUNG, K., ARNDT, S. & SEIBEL, C. 2002 Vaporization of multi component fuel droplets – numerical and experimental evaluation. In *Proceedings of the 18th Annual Conference Liquid Atomization & Spray Systems*. ILASS – Europe (Institute for Liquid Atomization and Spray Systems).

GIANNADAKIS, E., GAVAISES, M. & ARCOUMANIS, C. 2008*a* Modelling of cavitation in diesel injector nozzles. *J. Fluid Mech.* **616**, 153–193.

GIANNADAKIS, E., PAPOULIAS, D., THEODORAKAKOS, A. & GAVAISES, M. 2008*b* Simulation of cavitation in outward-opening piezo-type pintle injector nozzles. *Proc. Inst. Mech. Engrs,* D*: J. Automobile Engng* **222** (10), 1895–1910.

GMEHLING, J., KOLBE, B., KLEIBER, M. & RAREY, J. 2012 *Chemical Thermodynamics for Process Simulation*. Weinheim Wiley-VCH.

GRUNBERG, L. & NISSAN, A.H. 1949 Mixture law for viscosity. *Nature* **164**, 799–800.

HALLETT, W.L.H. & BEAUCHAMP-KISS, S. 2010 Evaporation of single droplets of ethanol–fuel oil mixtures. *Fuel* **89** (9), 2496–2504.

HALLETT, W.L.H. & LEGAULT, N.V. 2011 Modelling biodiesel droplet evaporation using continuous thermodynamics. *Fuel* **90** (3), 1221–1228.

HAO, Y., ZHANG, Y. & PROSPERETTI, A. 2017 Mechanics of gas–vapor bubbles. *Phys. Rev. Fluids* **2**, 034303.

HAYDUK, W. & MINHAS, B.S. 1982 Correlations for prediction of molecular diffusivities in liquids. *Can. J. Chem. Engng* **60** (2), 295–299.

HESSE, P.J., BATTINO, R., SCHARLIN, P. & WILHELM, E. 1996 Solubility of gases in liquids. 20. Solubility of He, Ne, Ar, Kr, N_2, O_2, CH_4, CF_4, and SF_6 in *n*-alkanes $n\text{-}C_lH_{2l+2}$ ($6 \geq l \geq 16$) at 298.15 K. *J. Chem. Engng Data* **41** (2), 195–201.

HIRSCHFELDER, J.O., CURTISS, C.F. & BYRD, R.B. 1969 *Molecular Theory of Gases and Liquids*. John Wiley & Sons.

HIRT, C.W., AMSDEN, A.A. & COOK, J.L. 1997 An arbitrary Lagrangian–Eulerian computing method for all flow speeds. *J. Comput. Phys.* **135** (2), 203–216.

HSIEH, D.Y. & PLESSET, M.S. 1961 Theory of rectified diffusion of mass into gas bubbles. *J. Acoust. Soc. Am.* **33** (2), 206–215.

HUANG, S. & MOHAMAD, A.A. 2009 Modeling of cavitation bubble dynamics in multicomponent mixtures. *Trans. ASME J. Fluids Engng* **131** (3), 031301.

ISDALE, J.D., MACGILLIVRAY, J.C. & CARTWRIGHT, G. 1985 Prediction of viscosity of organic liquid mixtures by a group contribution method. *Tech. Rep.*. National Engineering Laboratory.

JINBO, Y., KOBAYASHI, K., WATANABE, M. & TAKAHIRA, H. 2015 Numerical simulation of bubble collapse and the transfer of vapor and noncondensable gas through the bubble interface using the ghost fluid method. *J. Phys.: Conf. Ser.* **656**, 012021.

KAMATH, V. & PROSPERETTI, A. 1989 Numerical integration methods in gas-bubble dynamics. *J. Acoust. Soc. Am.* **85** (4), 1538–1548.

KAWASHIMA, H. & KAMEDA, M. 2008 Dynamics of a spherical vapor/gas bubble in varying pressure fields. *J. Fluid Sci. Technol.* **3** (8), 943–955.

KLEIN, A. & IBEN, U. 2010 Modeling of air release in liquids. In *7th International Conference Heat Transfer, Fluid Mechanics and Thermodynamics*. University of Pretoria.

KOLOVOS, K., KYRIAZIS, N., KOUKOUVINIS, P., VIDAL, A., GAVAISES, M. & MCDAVID, R.M. 2021 Simulation of transient effects in a fuel injector nozzle using real-fluid thermodynamic closure. *Appl. Energy Combust. Sci.* **7**, 100037.

KORETSKY, M.D. 2012 *Engineering and Chemical Thermodynamics*. Wiley.

KOUKOUVINIS, P., GAVAISES, M., LI, J. & WANG, L. 2016 Large eddy simulation of diesel injector including cavitation effects and correlation to erosion damage. *Fuel* **175**, 26–39.

LATINI, G. & PACETTI, M. 1977 The thermal conductivity of liquids: a critical review. In *Proceedings of the Fifteenth International Conference on Thermal Conductivity, Ottawa, ON, Canada*. Springer.

LEE, H.S. & MERTE, H. 1996 Spherical vapor bubble growth in uniformly superheated liquids. *Intl J. Heat Mass Transfer* **39** (12), 2427–2447.

LI, C.C. 1976 Thermal conductivity of liquid mixtures. *AIChE J.* **22** (5), 927–930.

LI, Y., DIDDENS, C., SEGERS, T., WIJSHOFF, H., VERSLUIS, M. & LOHSE, D. 2020 Rayleigh–Taylor instability by segregation in an evaporating multicomponent microdroplet. *J. Fluid Mech.* **899**, A22.

LI, Y., LV, P., DIDDENS, C., TAN, H., WIJSHOFF, H., VERSLUIS, M. & LOHSE, D. 2018 Evaporation-triggered segregation of sessile binary droplets. *Phys. Rev. Lett.* **120**, 224501.

LIEN, Y.C. 1969 Bubble growth rates at reduced pressure. Doctoral thesis, Massachusetts Institute of Technology.

LINSTROM, P.J. & MALLARD, W.G. (Ed.) 2016 *NIST Chemistry WebBook, NIST Standard Reference Database Number 69*. National Institute of Standards and Technology.

LIPPERT, A.M. & REITZ, R.D. 1997 Modeling of multicomponent fuels using continuous distributions with application to droplet evaporation and sprays. *SAE Tech. Paper* 972882.

MAIA DE OLIVEIRA, H.N., BEZERRA LOPES, F.W., DANTAS NETO, A.A. & CHIAVONE-FILHO, O. 2002 Vapor–liquid equilibria for pentane + dodecane and heptane + dodecane at low pressures. *J. Chem. Engng Data* **47** (6), 1384–1387.

MATSUMOTO, Y. & TAKEMURA, F. 1994 Influence of internal phenomena on gas bubble motion: effects of thermal diffusion, phase change on the gas–liquid interface and mass diffusion between vapor and noncondensable gas in the collapsing phase. *JSME Intl J. Ser.* B **37** (2), 288–296.

MATSUMOTO, Y. & YOSHIZAWA, S. 2005 Behaviour of a bubble cluster in an ultrasound field. *Intl J. Numer. Meth. Fluids* **47** (6–7), 591–601.

MIKIC, B.B., ROHSENOW, W.M. & GRIFFITH, P. 1970 On bubble growth rates. *Intl J. Heat Mass Transfer* **13** (4), 657–666.

MILLÁN-MERINO, A., FERNÁNDEZ-TARRAZO, E. & SÁNCHEZ-SANZ, M. 2021 Theoretical and numerical analysis of the evaporation of mono- and multicomponent single fuel droplets. *J. Fluid Mech.* **910**, A11.

NAJI MEIDANI, A.R. & HASAN, M. 1997 A numerical study of the complex dynamic behavior of a reactive gas bubble in water. *Appl. Math. Model.* **21** (3), 127–138.

NAJI MEIDANI, A.R. & HASAN, M. 2004 Mathematical and physical modelling of bubble growth due to ultrasound. *Appl. Math. Model.* **28** (4), 333–351.

NICKAEEN, M. 2020 Spatially resolved simulations of the non-equilibrium cavitation bubble dynamics including vapor and air transport. Doctoral thesis, Ruhr-Universität Bochum, Universitätsbibliothek.

NIGMATULIN, R.I. & KHABEEV, N.S. 1974 Heat exchange between a gas bubble and a liquid. *Fluid Dyn.* **9** (5), 759–764.

NIGMATULIN, R.I. & KHABEEV, N.S. 1975 Dynamics of vapor bubbles. *Fluid Dyn.* **10** (3), 415–421.

NIGMATULIN, R.I., KHABEEV, N.S. & NAGIEV, F.B. 1981 Dynamics, heat and mass transfer of vapour–gas bubbles in a liquid. *Intl J. Heat Mass Transfer* **24** (6), 1033–1044.

OERLEY, F., TRUMMLER, T., HICKEL, S., MIHATSCH, M.S., SCHMIDT, S.J. & ADAMS, N.A. 2015 Large-eddy simulation of cavitating nozzle flow and primary jet break-up. *Phys. Fluids* **27** (8), 086101.

PERKINS, L.R. & GEANKOPLIS, C.J. 1969 Molecular diffusion in a ternary liquid system with the diffusing component dilute. *Chem. Engng Sci.* **24** (7), 1035–1042.

PERSAD, A.H. & WARD, C.A. 2016 Expressions for the evaporation and condensation coefficients in the Hertz–Knudsen relation. *Chem. Rev.* **116** (14), 7727–7767.

PLESSET, M.S. 1970 Cavitation erosion in nonaqueous liquids. *Trans. ASME J. Basic Engng* **92** (4), 807–813.

PLESSET, M.S. & PROSPERETTI, A. 1977 Bubble dynamics and cavitation. *Annu. Rev. Fluid Mech.* **9** (1), 145–185.

PLESSET, M.S. & ZWICK, S.A. 1954 The growth of vapor bubbles in superheated liquids. *J. Appl. Phys.* **25** (4), 493–500.

POLING, B.E., O'CONNELL, J.P. & PRAUSNITZ, J.M. 2001 *The Properties of Gases and Liquids*. McGraw-Hill.

PROSPERETTI, A. 1991 The thermal behaviour of oscillating gas bubbles. *J. Fluid Mech.* **222**, 587–616.

PROSPERETTI, A. 2017 Vapor bubbles. *Annu. Rev. Fluid Mech.* **49** (1), 221–248.

PROSPERETTI, A. & PLESSET, M.S. 1978 Vapour-bubble growth in a superheated liquid. *J. Fluid Mech.* **85** (2), 349–368.

RA, Y. & REITZ, R.D. 2003 The application of a multicomponent droplet vaporization model to gasoline direct injection engines. *Intl J. Engine Res.* **4** (3), 193–218.

RACKETT, H.G. 1970 Equation of state for saturated liquids. *J. Chem. Engng Data* **15** (4), 514–517.

ROBINSON, A.J. & JUDD, R.L. 2004 The dynamics of spherical bubble growth. *Intl J. Heat Mass Transfer* **47** (23), 5101–5113.

ROKNI, H.B., GUPTA, A., MOORE, J.D., MCHUGH, M.A., BAMGBADE, B.A. & GAVAISES, M. 2019 Purely predictive method for density, compressibility, and expansivity for hydrocarbon mixtures and diesel and jet fuels up to high temperatures and pressures. *Fuel* **236**, 1377–1390.

SANDER, R. 2015 Compilation of Henry's Law constants (version 4.0) for water as solvent. *Atmos. Chem. Phys.* **15** (8), 4399–4981.

SAZHIN, S.S., ELWARDANY, A.E., KRUTITSKII, P.A., DEPRÉDURAND, V., CASTANET, G., LEMOINE, F., SAZHINA, E.M. & HEIKAL, M.R. 2011 Multi-component droplet heating and evaporation: numerical simulation versus experimental data. *Intl J. Therm. Sci.* **50** (7), 1164–1180.

SCHNERR, G., SCHMIDT, S.J., SEZAL, I.H. & THALHAMER, M. 2006 Shock and wave dynamics of compressible liquid flows with special emphasis on unsteady load on hydrofoils and on cavitation in injection nozzles. In *Proceedings of the 6th International Symposium on Cavitation, Invited Lecture*. Maritime Research Institute Netherlands.

SCHNERR, G.H. & SAUER, J. 2001 Physical and numerical modeling of unsteady cavitation dynamics. In *ICMF 4th International Conference on Multiphase Flow, New Orleans, USA*. Elsevier.

SCHRANK, K., MURRENHOFF, H. & STAMMEN, C. 2013 CFD simulations and experiments of the dispersed two-phase flow through hydraulic orifices. In *Proceedings of the ASME 2013 Fluids Engineering Division Summer Meeting*. American Society of Mechanical Engineers.

SKODA, R., IBEN, U., GÜNTNER, M. & SCHILLING, R. 2012 Comparison of compressible explicit density-based and implicit pressure-based CFD methods for the simulation of cavitating flows. In *Proceedings of the 8th International Symposium on Cavitation, Singapore*. Research Publishing Services.

SOCHARD, S., WILHELM, A.-M. & DELMAS, H. 1998 Gas–vapour bubble dynamics and homogeneous sonochemistry. *Chem. Engng Sci.* **53** (2), 239–254.

SOH, W.K. & KARIMI, A.A. 1996 On the calculation of heat transfer in a pulsating bubble. *Appl. Math. Model.* **20** (9), 638–645.

SPENCER, C.F. & DANNER, R.P. 1972 Improved equation for prediction of saturated liquid density. *J. Chem. Engng Data* **17** (2), 236–241.

STOREY, B.D. & SZERI, A.J. 1999 Mixture segregation within sonoluminescence bubbles. *J. Fluid Mech.* **396**, 203–221.

STOREY, B.D. & SZERI, A.J. 2000 Water vapour, sonoluminescence and sonochemistry. *Proc. R. Soc.* A **456** (1999), 1685–1709.

TAKEMURA, F. & MATSUMOTO, Y. 1994 Influence of internal phenomena on gas bubble motion: effects of transport phenomena and mist formation inside bubble in the expanding phase. *JSME Intl J. Ser.* B **37** (4), 736–745.

TAMIM, J. & HALLETT, W.L.H. 1995 A continuous thermodynamics model for multicomponent droplet vaporization. *Chem. Engng Sci.* **50** (18), 2933–2942.

THEODORAKAKOS, A., STROTOS, G., MITROGLOU, N., ATKIN, C. & GAVAISES, M. 2014 Friction-induced heating in nozzle hole micro-channels under extreme fuel pressurisation. *Fuel* **123**, 143–150.

VACHAPARAMBIL, K.J. & EINARSRUD, K.E. 2020 Numerical simulation of bubble growth in a supersaturated solution. *Appl. Math. Model.* **81**, 690–710.

VDI E.V. (Ed.) 1994 *VDI-Wärmeatlas, 7. Auflage*. VDI-Verlag GmbH.

VAN VELZEN, D., LOPES CARDOZO, R. & LANGENKAMP, H. 1972 Liquid viscosity and chemical constitution of organic compounds: a new correlation and a compilation of literature data. *Research Rep.* EUR 4735 e. Joint Nuclear Research Centre, Ispra Establishment, Italy.

VIDAL, A., RODRIGUEZ, C., KOUKOUVINIS, P., GAVAISES, M. & MCHUGH, M.A. 2020 Modelling of diesel fuel properties through its surrogates using perturbed-chain, statistical associating fluid theory. *Intl J. Engine Res.* **21** (7), 1118–1133.

VIGNES, A. 1966 Diffusion in binary solutions. Variation of diffusion coefficient with composition. *Ind. Engng Chem. Fundam.* **5** (2), 189–199.

WANG, G., XIE, Z. & TAN, Y. 1996*a* Nucleate pool boiling of pure liquids and binary mixtures. Part I. Analytical model for boiling heat transfer of pure liquids on smooth tubes. *J. Therm. Sci.* **5** (2), 104–111.

WANG, G., XIE, Z. & TAN, Y. 1996*b* Nucleate pool boiling of pure liquids and binary mixtures. Part II. Analytical model for boiling heat transfer of binary mixtures on smooth tubes and comparison of analytical models for both pure liquids and binary mixtures with experimental data. *J. Therm. Sci.* **5** (3), 201–209.

WATSON, K.M. 1943 Thermodynamics of the liquid state. *Ind. Engng Chem.* **35** (4), 398–406.

WILKE, C.R. & CHANG, P. 1955 Correlation of diffusion coefficients in dilute solutions. *AIChE J.* **1** (2), 264–270.

YAMAMOTO, K., KOBAYASHI, K., WATANABE, M., FUJII, H., KON, M. & TAKAHIRA, H. 2019 Influence of a small amount of noncondensable gas on shock wave generation inside a collapsing vapor bubble. *Phys. Rev. Fluids* **4**, 063603.

YANG, S. & REITZ, R. 2009 Integration of a continuous multi-component fuel evaporation model with an improved G-equation combustion and detailed chemical kinetics model with application to GDI engines. *SAE Tech. Paper* 2009-01-0722.

ZEIN, A., HANTKE, M. & WARNECKE, G. 2013 On the modeling and simulation of a laser-induced cavitation bubble. *Intl J. Numer. Meth. Fluids* **73** (2), 172–203.

ZHANG, L. & KONG, S.-C. 2012 Multicomponent vaporization modeling of bio-oil and its mixtures with other fuels. *Fuel* **95**, 471–480.

ZWART, P.J., GERBER, A.G. & BELAMRI, T. 2014 A two-phase flow model for predicting cavitation dynamics. In *Proceedings of the ICMF 2004 International Conference Multiphase Flow, Yokohama, Japan*. The Japanese Society for Multiphase Flow.